

Accurate electronic properties and intercalation voltages of olivine-type Li-ion cathode materials from extended Hubbard functionals

Iurii Timrov,^{1,*} Francesco Aquilante,¹ Matteo Cococcioni,² and Nicola Marzari^{1,3}

¹*Theory and Simulation of Materials (THEOS), and National Centre for Computational Design and Discovery of Novel Materials (MARVEL),*

École Polytechnique Fédérale de Lausanne (EPFL), CH-1015 Lausanne, Switzerland

²*Department of Physics, University of Pavia, via Bassi 6, I-27100 Pavia, Italy*

³*Laboratory for Materials Simulations, Paul Scherrer Institut, 5232 Villigen PSI, Switzerland*

(Dated: March 30, 2022)

The design of novel cathode materials for Li-ion batteries requires accurate first-principles predictions of structural, electronic, and magnetic properties as well as intercalation voltages in compounds containing transition-metal (TM) elements. For such systems, density-functional theory (DFT) with standard (semi-)local exchange-correlation functionals is of no use as it fails dramatically due to strong self-interaction (delocalization) errors for the partially filled d shells of the TMs. Here, we perform the first comparative study of the phospho-olivine cathode materials Li_xMnPO_4 , Li_xFePO_4 , and mixed-TM $\text{Li}_x\text{Mn}_{1/2}\text{Fe}_{1/2}\text{PO}_4$ ($x = 0, 1/4, 1/2, 3/4, 1$) using four electronic structure methods: DFT, DFT+ U , DFT+ $U+V$, and HSE06. We show that DFT+ $U+V$ outperforms the other three methods, provided that the on-site U and intersite V Hubbard parameters are determined from first-principles and self-consistently with respect to the structural parameters by means of density-functional perturbation theory (linear response). In particular, we demonstrate that DFT+ $U+V$ is the only method that correctly predicts the digital change in oxidation states of the TM ions in all compounds for the mixed-valence phases occurring at intermediate Li concentrations, leading to voltages in remarkable agreement with experiments. We thus show that the inclusion of intersite Hubbard interactions is essential for the accurate prediction of thermodynamic quantities when electronic localization occurs while in the presence of inter-atomic orbital hybridization. At variance with the other methods, DFT+ $U+V$ alone is capable to describe such localization-hybridization interplay, and thus opens the door for the study of more complex cathode materials as well as for a reliable exploration of the chemical space of compounds for Li-ion batteries.

I. INTRODUCTION

Recent years have witnessed urgent need in the renewable energy and the availability of energy storage technology that is needed at all scales. One of the major advances in this area can be traced back to the development of Li-ion rechargeable batteries [1, 2] that are currently employed in a variety of application, e.g. for portable electronics, power tools, automotive industry, electricity grids, to name a few [3, 4]. These technologies are in increasing demand due to a global increase in energy consumption, widening dependence on the availability of efficient, safe, and non-toxic Li-ion batteries.

The properties and performance of Li-ion batteries (such as power and energy density, capacity retention, cyclability, thermal stability, etc.) depend on many factors and their interplay within the complexity of the actual multi-component device. As part of this network, cathode materials play a pivotal role, determining the Li intercalation voltage and cyclability of Li^+ ions through the interface with the electrolyte. There are various types of cathode materials, among which we mention layered, spinel, olivine, prussian blue, and cation-disordered rock-salt [5–7]. A key ingredient of cathodes are transition-metal (TM) elements that are electrochemically active

species that are changing their oxidation state during charging and discharging of the battery. It is therefore of paramount importance to understand at the atomistic level what properties of such compounds lead to efficient electrochemical processes.

An important tool for studying cathode materials is density-functional theory (DFT) [8, 9], which is a workhorse for first-principles simulations in physics, chemistry, and materials science. DFT requires approximations to the exchange-correlation (xc) functional, with local spin-density approximation (LSDA) and spin-polarized generalized-gradient approximation (σ -GGA) being the most popular ones. However, these are unable to provide satisfactory results for many TM compounds due to large self-interaction errors (SIE) [10, 11] which are especially large for localized d and f electrons. For this reason, more accurate approaches beyond “standard DFT” (i.e. based on LSDA or σ -GGA) are generally used, among which we mention Hubbard-corrected DFT (so-called DFT+ U [12–14] and its extension DFT+ $U+V$ [15–17]), DFT with hybrid functionals (e.g. PBE0 [18] and HSE06 [19, 20]), DFT with meta-GGA functionals such as SCAN [21] and its flavors [22, 23], to name a few. In DFT+ U , the Hubbard U correction is applied selectively only to the partially filled d states of TM elements to alleviate SIE for these states [24], while all other states are treated at the level of LSDA or σ -GGA. In contrast, in hybrid functionals a

* iurii.timrov@epfl.ch

fraction of exact exchange (EXX) is added (25% in the case of PBE0 and HSE06) and the remainder of exchange is treated at the σ -GGA level, together with 100% of the σ -GGA correlation. Finally, in meta-GGA functionals the gradient of the kinetic energy density is taken into account and known exact constraints are satisfied (17 in the case of SCAN) [25]. In the context of first-principle prediction of the properties of cathode materials, it still remains to establish which of these classes of advanced functionals provides the most accurate, reliable, and computationally affordable results.

The major interest in the use of DFT+ U and DFT+ U + V comes from their ability to greatly improve the accuracy of standard DFT at only a marginal increase in the computational cost [26]. However, this is true only if the proper values of the on-site U and intersite V Hubbard parameters are made available. In practice, these are unknown *a priori* and need to be determined by means of a robust protocol. One possibility, still widespread, is to assign *bona fide* empirical values to the Hubbard parameters. However, a much more robust and meaningful approach is to compute such parameters by means of first-principle methods [27], such as constrained DFT (cDFT) [28–36], Hartree-Fock based approaches [16, 17, 37–40], and the constrained random phase approximation (cRPA) [41–44]. In particular, a linear-response formulation [45] of cDFT (LR-cDFT) has become a method of choice for many computational DFT+ U (+ V) studies; moreover, its recent reformulation in terms of density-functional perturbation theory (DFPT) [19, 21] further boosted its success thanks to the fact that it allows to replace computationally expensive supercells by a primitive cell with monochromatic perturbations, thus significantly reducing the computational burden of determining Hubbard parameters. DFT+ U with Hubbard U computed using LR-cDFT [36, 48–50] or cRPA [51] has proven to be effective in improving intercalation voltages and electronic structure properties of cathode materials, and, remarkably, DFT+ U + V with U and V determined from LR-cDFT in a self-consistent fashion [21] was shown to provide excellent agreement with experimental voltages for olivine-type cathode materials [22] thus highlighting the importance of inter-site Hubbard V interactions.

Hybrid functionals exhibit a similar accuracy improvement over standard DFT as they work in the same direction of reducing SIE for TM compounds. At variance with Hubbard functionals, however, their use comes at a much higher computational cost than standard DFT. Furthermore, for hybrid functionals, quite often the required fraction of exact exchange must be tuned in solids in order to reach satisfactory agreement with experiments. Although, there are ways to determine *ab initio* the optimal amount of exact exchange needed for a given system of interest [53–58], very often the use of tuned hybrid functional tends to deviate considerably from a pure first-principle based practice. If one disregards the option of tuning the amount of EXX exchange, it remains the

possibility to choose the hybrid functional upon considerations on its reliability for the problem of interest. In particular, for the study of cathode materials HSE06 has proven its ability to predict accurate electronic and electrochemical properties of some pivotal examples of such materials, e.g. for the phospho-olivine Li_xMnPO_4 [59] and the spinel $\text{Li}_x\text{Mn}_2\text{O}_4$ [60] compounds.

In this paper, we present a detailed comparative study for selected olivine-type cathode materials: Li_xFePO_4 , Li_xMnPO_4 , as well as the more complex mixed-TM compound $\text{Li}_x\text{Mn}_{1/2}\text{Fe}_{1/2}\text{PO}_4$ ($x = 0, 1/4, 1/2, 3/4, 1$). We perform calculations with four electronic-structure methods: DFT, DFT+ U , DFT+ U + V , and HSE06, with the aim to assess the reliability of their predictions (e.g., oxidation states and Li intercalation voltages) in comparison with experiments. We show that DFT+ U + V remarkably outperforms the other three well-established methods. Key requirement is that the on-site U and intersite V Hubbard parameters are determined from first-principles self-consistently using DFPT [19, 21]. In particular, we demonstrate that DFT+ U + V accurately predicts the electronic structure not only for the fully delithiated/lithiated compounds ($x = 0, 1$), but also for the intermediate Li concentrations ($x = 1/4, 1/2, 3/4$). Overall, HSE06 and DFT+ U results are in good qualitative agreement with DFT+ U + V , and superior to standard DFT, but intercalation voltages do not match the quantitative accuracy shown by DFT+ U + V . Importantly, DFT+ U + V predicts a digital change in atomic occupations when gradually changing the Li concentration while DFT averages out the occupations over sites and HSE06 shows a less clear pattern in the digital change of occupations for Fe-containing phospho-olivines. This study shows that the inclusion of intersite interactions V is essential for the accurate prediction of thermodynamic quantities when electronic localization occurs in the presence of significant inter-atomic hybridization, confirming and enriching the findings of earlier work by some of us [22].

The paper is organized as follows. Section II presents the theoretical framework with the basics of HSE06, DFT+ U , and DFT+ U + V , and the linear-response calculation of U and V using DFPT. In Sec. III we present our findings for the oxidation states, Löwdin occupations, spin-resolved projected density of states (PDOS), and voltages; and in Sec. IV we provide the conclusions.

II. METHODS

In this section we discuss the basics of HSE06 [19, 20], DFT+ U [12, 14], and DFT+ U + V [15, 26] as well as the main idea of the DFPT approach for computing Hubbard parameters [19, 21]. In the following, we will use the generic name “DFT+Hubbard” as broadly referring to any flavor of Hubbard-corrected DFT, which in this paper covers DFT+ U and DFT+ U + V . For the sake of simplicity, the formalism is presented in the framework of

norm-conserving (NC) PPs in the collinear spin-polarized case. Hartree atomic units are used throughout.

A. DFT+Hubbard

For the sake of generality, here we discuss the DFT+ U + V formalism [15]. It can be easily simplified to DFT+ U by setting $V = 0$. In DFT+ U + V , the xc functional consists of the DFT energy that is computed using e.g. PBE or any other (semi-)local functional and a corrective Hubbard term [15]:

$$E_{\text{xc}}^{\text{PBE}+U+V} = E_{\text{xc}}^{\text{PBE}} + E_{\text{xc}}^{U+V}, \quad (1)$$

where E_{xc}^{U+V} is the Hubbard energy that removes SIE (in the Hubbard manifold) present due to the use of approximate xc functionals such as PBE. At variance with the DFT+ U approach that contains only onsite interactions scaled by U , DFT+ U + V contains also intersite interactions between orbitals centered on different sites scaled by V . In the simplified rotationally-invariant formulation, the extended Hubbard term E_{xc}^{U+V} is defined such that it removes the mean-field PBE-based interactions in the Hubbard manifold and adds the ones that restore the piece-wise linear energy behavior [26], and it reads [15]:

$$E_{\text{xc}}^{U+V} = \frac{1}{2} \sum_I \sum_{\sigma m m'} U^I (\delta_{mm'} - n_{mm'}^{II\sigma}) n_{m'm}^{II\sigma} - \frac{1}{2} \sum_I \sum_{J(J \neq I)}^* \sum_{\sigma m m'} V^{IJ} n_{mm'}^{IJ\sigma} n_{m'm}^{JI\sigma}, \quad (2)$$

where I and J are atomic site indices, m and m' are the magnetic quantum numbers associated with a specific angular momentum, U^I and V^{IJ} are the effective onsite and intersite Hubbard parameters, and the star in the sum denotes that for each atom I , the index J covers all its neighbors up to a given distance (or up to a given shell). The generalized occupation matrices $n_{mm'}^{IJ\sigma}$ are based on a projection of the KS wavefunctions on localized orbitals $\varphi_m^I(\mathbf{r})$ of neighbor atoms [15]:

$$n_{mm'}^{IJ\sigma} = \sum_{v,\mathbf{k}} f_{v,\mathbf{k}}^\sigma \langle \psi_{v,\mathbf{k}}^\sigma | \varphi_{m'}^J \rangle \langle \varphi_m^I | \psi_{v,\mathbf{k}}^\sigma \rangle, \quad (3)$$

where $f_{v,\mathbf{k}}^\sigma$ are the occupations of the KS states, and $\varphi_m^I(\mathbf{r}) \equiv \varphi_m^{\gamma(I)}(\mathbf{r} - \mathbf{R}_I)$ are localized orbitals centered on the I th atom of type $\gamma(I)$ at the position \mathbf{R}_I . It is convenient to establish a short-hand notation for the onsite occupation matrix: $n_{mm'}^{II\sigma} \equiv n_{mm'}^{II\sigma}$, which is used in DFT+ U that corresponds to the first line of Eq. (2). The two terms in Eq. (2) (i.e., proportional to the onsite U^I and intersite V^{IJ} couplings) counteract each other: the onsite term favors localization on atomic sites (thus suppressing hybridization with neighbors), while the intersite term favors hybridized states with components on neighbor atoms (thus suppressing the onsite localization).

It is the balance between these two competing effects that determines the ground state of the system - an accurate evaluation of U^I and V^{IJ} is crucial in this respect.

In DFT+Hubbard the values of the Hubbard parameters are not known *a priori*, and hence very often these values are adjusted empirically such that the final results of simulations match some experimental properties of interest (e.g. band gaps, oxidation enthalpies, etc.). This is fairly arbitrary, which makes DFT+Hubbard not fully first-principles and, most importantly, not predictive. Therefore, first-principles calculation of Hubbard parameters is essential and highly desirable. The aforementioned LR-cDFT approach allows to compute U and V from a generalized piece-wise linearity condition [15, 45]. Within this framework the Hubbard parameters are the elements of an effective interaction matrix computed as the difference between bare and screened inverse susceptibilities [45]:

$$U^I = (\chi_0^{-1} - \chi^{-1})_{II}, \quad (4)$$

$$V^{IJ} = (\chi_0^{-1} - \chi^{-1})_{IJ}. \quad (5)$$

The susceptibility matrices χ_0 and χ measure the response of atomic occupations to a shift in the potential acting on the atomic states of a specific Hubbard atom [45]: $\chi_{IJ} = \sum_{m\sigma} (dn_{mm'}^{I\sigma}/d\alpha^J)$. The difference between χ_0 and χ consists in the fact that the former represents the (bare) response to the total potential, while the latter - the (total) response to the external potential [61]. In order to avoid computationally demanding supercell calculations, required within the LR-cDFT approach to make the perturbation isolated, we have recently recast the LR calculation outlined above within DFPT, so that the response to isolated perturbations can be efficiently computed from the superposition of the variation of atomic occupations to monochromatic (i.e., wavevector-specific) perturbations using primitive cells [19]:

$$\frac{dn_{mm'}^{I\sigma}}{d\alpha^J} = \frac{1}{N_{\mathbf{q}}} \sum_{\mathbf{q}} e^{i\mathbf{q} \cdot (\mathbf{R}_I - \mathbf{R}_{I'})} \Delta_{\mathbf{q}}^{s'} n_{mm'}^{s\sigma}. \quad (6)$$

Here, $\Delta_{\mathbf{q}}^{s'} n_{mm'}^{s\sigma}$ is the response of the occupation matrix, $I \equiv (l, s)$ and $J \equiv (l', s')$, where s and s' are the atomic indices in unit cells while l and l' are the unit-cell indices. \mathbf{R}_l and $\mathbf{R}_{l'}$ are the Bravais lattice vectors, and the grid of \mathbf{q} points is chosen fine enough to make the resulting atomic perturbations effectively decoupled from their periodic replicas. An exhaustive illustration of this approach can be found in Refs. [19, 21], also discussing a recent extension to ultrasoft and PAW pseudopotentials.

It is crucial to keep in mind that the values of the computed Hubbard parameters dependent strongly on the type of Hubbard projector functions $\varphi_m^I(\mathbf{r})$ that are used in DFT+Hubbard [13, 24, 62, 63]. Here we employ orthogonalized atomic orbitals that are computed using the

Löwdin orthogonalization method [11, 12]:

$$\varphi_m^I(\mathbf{r}) = \sum_{jm'} \left(\hat{O}^{-\frac{1}{2}} \right)_{m'm}^{JI} \phi_{m'}^J(\mathbf{r}), \quad (7)$$

where \hat{O} is the orbital overlap matrix, whose matrix elements are defined as: $(\hat{O})_{mm'}^{IJ} = \langle \phi_m^I | \phi_{m'}^J \rangle$, and $\phi_m^I(\mathbf{r})$ are the nonorthogonalized atomic orbitals provided with PPs. With this choice of projector functions the electrons in the intersite overlap regions are not counted twice when computing the atomic occupations used in the Hubbard correction, as it is instead the case for the nonorthogonalized atomic orbitals $\phi_m^I(\mathbf{r})$. As a matter of fact, DFT+Hubbard with the Löwdin orthogonalized orbitals have proven to give more accurate results for various properties of materials [67–72], provided the Hubbard parameters are consistently computed with the Löwdin orthogonalized orbitals. Therefore, Hubbard parameters and Hubbard projectors should always be defined consistently and reported together.

B. HSE06

In a range-separated hybrid functional HSE06 the exchange energy is divided into a short-range (SR) and a long-range (LR) part. Only 25% of the SR part consists of the EXX energy and the remaining 75% is the PBE exchange energy, while the LR exchange part is fully computed at the PBE level [19, 20]. The total xc energy is

$$E_{xc}^{\text{HSE06}} = \frac{1}{4} E_x^{\text{EXX,SR}} + \frac{3}{4} E_x^{\text{PBE,SR}} + E_x^{\text{PBE,LR}} + E_c^{\text{PBE}}, \quad (8)$$

where E_c^{PBE} is the PBE correlation energy. The EXX SR energy is the most computationally expensive term and it is defined by generalizing the definition of EXX [73] as follows:

$$E_x^{\text{EXX,SR}} = -\frac{1}{2} \sum_{\sigma} \sum_{v,\mathbf{k}} \sum_{v',\mathbf{k}'} \int \int d\mathbf{r} d\mathbf{r}' \text{erfc}(\omega|\mathbf{r}-\mathbf{r}'|) \times \frac{\psi_{v,\mathbf{k}}^{\sigma*}(\mathbf{r}) \psi_{v',\mathbf{k}'}^{\sigma'}(\mathbf{r}) \psi_{v',\mathbf{k}'}^{\sigma'*}(\mathbf{r}') \psi_{v,\mathbf{k}}^{\sigma}(\mathbf{r}')}{|\mathbf{r}-\mathbf{r}'|}, \quad (9)$$

where erfc is the complementary error function, $\omega = 0.106 a_0$ is the screening parameter with a_0 being the Bohr radius [20], v and σ represent, respectively, the band and spin labels of the Kohn-Sham (KS) wavefunctions $\psi_{v,\mathbf{k}}^{\sigma}(\mathbf{r})$ (normalized to unity in the primitive cell), \mathbf{k} indicate points in the first Brillouin zone. The EXX SR energy of Eq. (9) describes only exchange interactions at relatively short atomic length scales, and it corresponds to “onsite exchange” and “intersite exchange” energy contributions: the former describes exchange acting between orbitals centered on the same atom while the latter describes exchange acting between orbitals centered on different atoms [60]. This aspect is crucial and in the following we will further investigate such analogy between

HSE06 and DFT+Hubbard.

C. HSE06 vs. DFT+Hubbard

It is instructive to establish analogies between the hybrid functional HSE06 and DFT+Hubbard [74]. It has been shown in Refs. [16, 17] that DFT+ $U+V$ predicts the electronic structure of TM compounds and light-element compounds in closer agreement with HSE06 with respect to DFT+ U . However, the origin of this improvement was not investigated in detail. As will be shown in what follows, DFT+ $U+V$ outperforms HSE06 in accuracy also for predicting electronic properties and voltages in phospho-olivines, and we provide a simple qualitative explanation for this.

DFT+ U and hybrid functionals share one important feature: they both attempt to correct SIE for orbitals centered on the same site. However, in contrast to HSE06, DFT+ U does not correct for SIE originating from the interactions of orbitals centered on different (neighboring) sites. This is why for systems with covalent bonding DFT+ U typically disagrees with HSE06 predictions. In contrast, this latter effect is captured by DFT+ $U+V$, which makes it more general and allows to cover similar physics as the one described by HSE06. However, it is important to recall that in DFT+ $U+V$ only a subset of orbitals are corrected while hybrid functionals act on all the orbitals. Moreover, since typically only nearest-neighbor inter-site interactions are taken into account in DFT+ $U+V$, this looks similar to HSE06 which has only the EXX SR, while long-range effects are fully disregarded both in DFT+ $U+V$ and HSE06.

D. Crystal structure, magnetic ordering, and further calculation details

The phospho-olivines Li_xFePO_4 , Li_xMnPO_4 , and $\text{Li}_x\text{Mn}_{1/2}\text{Fe}_{1/2}\text{PO}_4$ have an orthorhombic crystal structure at $x = 0$ and $x = 1$ with a $Pnma$ space group [23–25]. The unit cell contains four formula units, i.e. 24 atoms in the case of $x = 0$ and 28 atoms in the case of $x = 1$. The crystal structure at $x = 1$ is shown in Fig. 1. The TM atoms (labeled as M with an index from 1 to 4 in Fig. 1) are coordinated by six O atoms forming a MO_6 octahedron of which it occupies the center. The P atoms are instead at the center of PO_4 tetrahedra that they form with neighboring oxygens. The three-dimensional structure of the crystal can be understood as being based on a network of corner-sharing MO_6 octahedra further linked by “interstitial” PO_4 tetrahedra that act as structural reinforcer [avoiding excessive volume variations upon Li (de-)intercalation] and chemical stabilizers (useful to avoid oxygen escapes). Li ions reside within octahedral channels along the intermediate-length side of the cell.

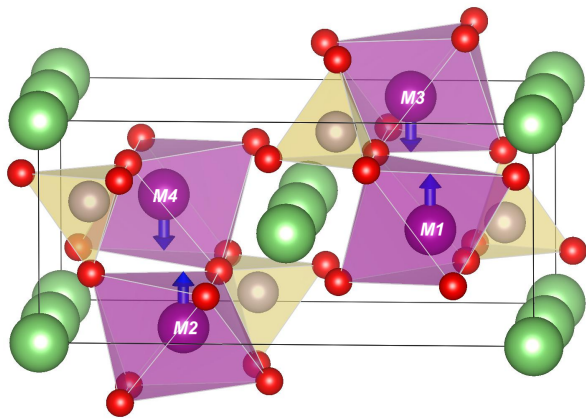


FIG. 1: Crystal structure of phospho-olivines.

Transition-metal elements ($M1-M4$) are indicated in purple, O atoms in red, Li atoms in green, and P atoms in yellow. Blue vertical arrows indicate the orientation of spin. In Li_xMnPO_4 , $M1-M4$ correspond to Mn1–Mn4, in Li_xFePO_4 , $M1-M4$ correspond to Fe1–Fe4, and in $\text{Li}_x\text{Mn}_{1/2}\text{Fe}_{1/2}\text{PO}_4$: $M1=\text{Fe}1$, $M2=\text{Mn}2$, $M3=\text{Fe}3$, $M4=\text{Mn}4$.

The phospho-olivines are known to show an anti-ferromagnetic behavior below their transition temperatures [27–29, 79]. In the previous study (Ref. [22]) it was shown that different antiferromagnetic arrangements of spins result in total energies that differ not more than by ~ 20 meV at the DFT+Hubbard level of theory. In this paper we use the magnetic configuration that minimizes the total energy (labeled “AF₁” in Ref. [22]), and it is depicted in Fig. 1. Moreover, we use the same spin arrangement in the mixed TM phospho-olivine $\text{Li}_x\text{Mn}_{1/2}\text{Fe}_{1/2}\text{PO}_4$. Finally, there are several configurations for arranging two Mn and two Fe atoms in the unit cell of $\text{Li}_x\text{Mn}_{1/2}\text{Fe}_{1/2}\text{PO}_4$. Our goal here is not to investigate all configurations but rather to choose one as a representative case for comparing results obtained using different levels of theory (see Sec. II). To this end, we choose to arrange Mn and Fe atoms such that two Mn atoms are antiferromagnetically coupled to each other and same for Fe atoms, as shown in Fig. 1.

All technical details of the calculations are described in Sec. S1 of the Supplemental Material (SM) [82]. Hubbard parameters were computed self-consistently using DFPT as described in Sec. II, and their values are listed in Sec. S2 of SM [82]. The crystal structure was optimized using DFT and DFT+Hubbard, and the results are reported in Sec. S3 of SM [82]; for HSE06 calculations we have used the DFT+ U + V geometry since the structural optimization at the HSE06 level is computationally too expensive. Other properties reported in the SM will be mentioned in Sec. III.

III. RESULTS AND DISCUSSION

A. Oxidation states, Löwdin occupations, and magnetic moments

The concept of oxidation state (OS) is central and ubiquitous in chemistry and physics, it is widely used to describe redox reactions, electrolysis, and many electrochemical processes as it allows to track electron movement during reactions [84]. The main idea is that the variations in electron number must be integer and this assigns the OS of an ion [85]. However, OS has long eluded a proper quantum-mechanical interpretation. Numerous methods have been proposed to determine the OS, and such methods often infer the OS of ions from schemes for allocating charges to ions. These schemes can be classified into categories, among which we mention: *i*) partition of space with integration of the total charge density within space allocated to each ion (e.g. Bader [86] and Voronoi [87] charges), and *ii*) projection of the electronic wavefunctions onto a localized basis (e.g. Mulliken [88] and Löwdin [11] charges, or natural bond orbitals [89]). On the one hand, in the partition schemes all orbitals contribute to the charge within the allocated volume (e.g. a sphere of a certain radius centered on an ion), thus losing the connection to the OS of individual ions and its certain manifold (e.g. d orbitals of TM elements). On the other hand, in the projection schemes there is dependence on the type of projector functions that are used to construct the localized basis set (and dependence on cutoffs used in some methods). The electronic populations computed using these methods are quite useful to give an indication of the OS, however these populations are often noninteger and their changes during redox reactions are significantly smaller than the changes in the nominal electron numbers for the end elements of the reaction. Raebiger et al. [90] have pointed out that the net physical charge belonging to a TM atom is essentially independent of its OS and this is due to the negative-feedback charge regulation mechanism that is inherent to TM compounds [91, 92]. The difficulty in accurate and unambiguous determination of the OS of ions has inspired the development of novel methods. Among these, we highlight the method of Ref. [93] which is based on wavefunction topology and the modern theory of polarization, and the method of Ref. [26] which is the projection-based method that uses eigenvalues of the atomic occupation matrix to determine the OS. Whereas the OS as defined in Ref. [93] has proven to be effective for transport processes [94], here we choose to adopt the method of Ref. [26] which is particularly well suited for the purpose of the present work.

Table I reports the population analysis data for the $3d$ shell of Mn and Fe atoms in Li_xMnPO_4 and Li_xFePO_4 at $x = 0$ and $x = 1$ computed using four levels of theory (DFT, DFT+ U , DFT+ U + V , and HSE06) and the nominal data. More specifically, it shows the eigenvalues of the site-diagonal ($I = J$) atomic occupation

Material	Method	x	λ_1^\uparrow	λ_2^\uparrow	λ_3^\uparrow	λ_4^\uparrow	λ_5^\uparrow	λ_1^\downarrow	λ_2^\downarrow	λ_3^\downarrow	λ_4^\downarrow	λ_5^\downarrow	n	m (μ_B)	OS
Li_xMnPO_4	DFT	0	0.42	0.98	0.99	0.99	0.99	0.09	0.10	0.13	0.16	0.27	5.12	3.63	3+
		1	0.99	0.99	0.99	1.00	1.00	0.03	0.04	0.05	0.10	0.11	5.28	4.62	2+
	DFT+ U	0	0.54	0.99	0.99	1.00	1.00	0.04	0.05	0.06	0.08	0.19	4.95	4.10	3+
		1	0.99	0.99	1.00	1.00	1.00	0.02	0.02	0.03	0.07	0.08	5.19	4.76	2+
	DFT+ U + V	0	0.50	0.99	0.99	1.00	1.00	0.05	0.06	0.08	0.09	0.22	4.98	3.97	3+
		1	0.99	0.99	1.00	1.00	1.00	0.02	0.02	0.03	0.07	0.08	5.21	4.75	2+
	HSE06	0	0.40	0.99	0.99	0.99	0.99	0.06	0.07	0.09	0.10	0.23	4.91	3.83	3+
		1	0.99	0.99	1.00	1.00	1.00	0.02	0.02	0.03	0.07	0.08	5.21	4.75	2+
	Nominal	0	0.00	1.00	1.00	1.00	1.00	0.00	0.00	0.00	0.00	0.00	4.00	4.00	3+
		1	1.00	1.00	1.00	1.00	1.00	0.00	0.00	0.00	0.00	0.00	5.00	5.00	2+
Li_xFePO_4	DFT	0	0.97	0.98	0.99	1.00	1.00	0.15	0.16	0.17	0.25	0.26	5.93	3.94	3+
		1	0.99	0.99	0.99	0.99	1.00	0.06	0.07	0.13	0.14	0.98	6.32	3.57	2+
	DFT+ U	0	0.99	0.99	1.00	1.00	1.00	0.09	0.10	0.10	0.22	0.24	5.72	4.22	3+
		1	0.99	0.99	1.00	1.00	1.00	0.02	0.04	0.08	0.09	1.00	6.20	3.76	2+
	DFT+ U + V	0	0.99	0.99	1.00	1.00	1.00	0.09	0.12	0.12	0.21	0.25	5.76	4.18	3+
		1	0.99	0.99	1.00	1.00	1.00	0.03	0.04	0.09	0.10	0.99	6.22	3.74	2+
	HSE06	0	0.99	0.99	0.99	0.99	1.00	0.09	0.10	0.10	0.19	0.23	5.67	4.26	3+
		1	0.99	0.99	1.00	1.00	1.00	0.03	0.04	0.09	0.09	0.99	6.22	3.74	2+
	Nominal	0	1.00	1.00	1.00	1.00	1.00	0.00	0.00	0.00	0.00	0.00	5.00	5.00	3+
		1	1.00	1.00	1.00	1.00	1.00	0.00	0.00	0.00	0.00	1.00	6.00	4.00	2+

TABLE I: Population analysis data for the $3d$ shell of Mn and Fe atoms in Li_xMnPO_4 and Li_xFePO_4 at $x = 0$ and $x = 1$ computed using four levels of theory (DFT, DFT+ U , DFT+ U + V , and HSE06) and the nominal data. This table shows the eigenvalues of the site-diagonal occupation matrix for the spin-up (λ_i^\uparrow , $i = \overline{1, 5}$) and spin-down (λ_i^\downarrow , $i = \overline{1, 5}$) channels, Löwdin occupations $n = \sum_i (\lambda_i^\uparrow + \lambda_i^\downarrow)$, magnetic moments $m = \sum_i (\lambda_i^\uparrow - \lambda_i^\downarrow)$, and the oxidation state (OS). For the sake of simplicity we dropped the atomic site index I from all quantities reported here. The eigenvalues are written in the ascending order (from left to right) for each spin channel. The eigenvalues written in bold are considered as being such that correspond to fully occupied states and thus are taken into account when determining the OS according to Ref. [26].

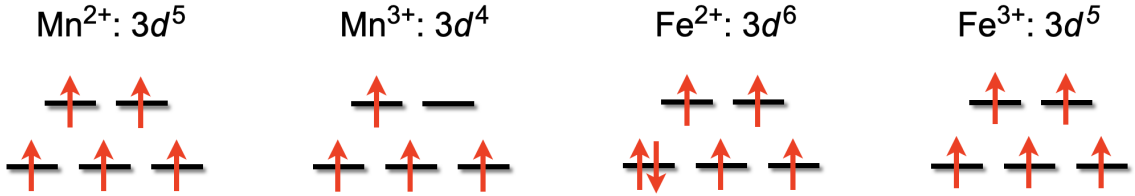


FIG. 2: Nominal occupations of the $3d$ manifold of Mn and Fe atoms (not hybridized with ligands) in a high-spin undistorted octahedral complex with different oxidation states. The t_{2g} and e_g levels are indicated with black horizontal lines and are nondegenerate due to the crystal-field splitting; up and down red arrows correspond to spin-up and spin-down electrons, respectively.

matrix $n_{mm'}^{I\sigma}$ of size 5×5 [see Eq. (3)] in the spin-up ($\sigma = \uparrow : \lambda_i^\uparrow$) and spin-down ($\sigma = \downarrow : \lambda_i^\downarrow$) channels, Löwdin occupations $n = \sum_{i=1}^5 (\lambda_i^\uparrow + \lambda_i^\downarrow)$, magnetic moments $m = \sum_{i=1}^5 (\lambda_i^\uparrow - \lambda_i^\downarrow)$, and the OS determined using the method of Ref. [26]. The same analysis has been performed for $\text{Li}_x\text{Mn}_{1/2}\text{Fe}_{1/2}\text{PO}_4$ at $x = 0$ and 1 and is discussed in Sec. S4 in SM [82]; we do not show these results here since they are similar to those presented in Table I. As can be seen from the eigenvalues in Table I, the allocated charge on the $3d$ shell of TM ions (Fe and Mn) contains contributions from both the fully occupied

d orbitals (i.e. the eigenvalues that are close to 1.0 [95] and are shown in bold) and the contributions due to the mixing of the formally empty d orbitals with the ligand orbitals (O- $2p$ states) that results in fractional occupations of these d states. According to Ref. [26], in order to determine the OS we need to count how many d states are “fully occupied”; by following this procedure and recalling what is the valence electronic configuration of TM atoms considered here (Mn: $3d^5 4s^2$ and Fe: $3d^6 4s^2$) we readily find that in the fully delithiated olivines ($x = 0$) the OS of Mn and Fe is 3+ while in the fully lithiated olivines ($x = 1$) the OS of Mn and Fe is 2+. This agrees well with

the nominal OS shown in Table I and depicted in Fig. 2. Thus, we find that Mn and Fe are in a high-spin state in agreement with experiments [27, 29, 96]. Different levels of theory considered here give slightly different occupations of the formally empty d states: For instance, in LiMnPO_4 the unoccupied d state in the spin-up channel (corresponding to λ_1^\uparrow) gets filled in the range from 0.40 to 0.54 due to mixing with O-2 p ligand states, whereas much smaller filling of all d states occurs in the spin-down channel. Therefore, a larger deviation from 0 of the eigenvalues indicates a stronger mixing of the unoccupied d orbitals with the ligand orbitals, in accordance with the prescription of Ref. [26].

Table I contains also the Löwdin occupations n and magnetic moments m , which are often used to determine the OS of ions. However, as we discussed earlier, these are not always appropriate descriptors of the OS: due to the hybridization of the TM orbitals with the ligand orbitals, it is difficult to assign the correct number of electrons to the TM ion, and moreover the number of electrons remains nearly unchanged for the TM ions upon the process of (de-)lithiation due the negative-feedback charge regulation mechanism [90]. Indeed, from Table I we can see that e.g. for FePO_4 and LiFePO_4 the nominal Löwdin occupations are 5.0 and 6.0, respectively, while the computational predictions on average give 5.8 and 6.2 (with DFT giving the largest deviations from the nominal occupations due to SIE). Magnetic moments are also often used to determine the OS, but here we can see that these are also not appropriate quantities: the nominal magnetic moments for FePO_4 and LiFePO_4 are 5.0 and 4.0 μ_B , respectively, while the computational predictions on average give 4.2 and 3.7 μ_B (with DFT again giving the largest deviations from the nominal magnetic moments due to SIE). It is interesting to note that DFT+ U + V predicts the Löwdin occupations and magnetic moments in remarkable agreement with the HSE06 ones for LiFePO_4 , while for FePO_4 the DFT+ U results are closer to HSE06 than the DFT+ U + V ones. Similar trends are also observed for MnPO_4 and LiMnPO_4 , which suggests that the TM-ligand inter-site electronic interactions are slightly stronger in the fully lithiated olivines. Nevertheless, the Löwdin occupations (and magnetic moments) are still very useful quantities for bookkeeping [90], in particular when describing the gradual (de-)lithiation process as discussed in the following.

Figure 3 shows the Löwdin occupations of the $3d$ shell of Mn and Fe atoms in Li_xMnPO_4 , Li_xFePO_4 , and $\text{Li}_x\text{Mn}_{1/2}\text{Fe}_{1/2}\text{PO}_4$ at $x = 0, 1/4, 1/2, 3/4, 1$ computed using three levels of theory (DFT, DFT+ U + V , and HSE06). Here we do not show the DFT+ U results since these are known to be less accurate than the DFT+ U + V ones in olivines e.g. for $x = 1/2$ [22]; in addition, the simultaneous convergence of the Hubbard U parameters within DFT+ U and the crystal structure in a self-consistent fashion [68] is problematic for $x = 1/4$ and $3/4$ (which requires further investigation). We stress that no convergence issues were found when using self-

consistent DFT+ U + V . Our main goal here is to compare the accuracy of the DFT+ U + V approach versus the well-established HSE06 one. In the case of Li_xMnPO_4 , we can see that DFT+ U + V and HSE06 agree remarkably well and both show a “digital” change in the Löwdin occupations: adding one Li^+ ion and one electron to the cathode during the lithiation process leads to changes in the occupation from 4.98 to 5.21 and change in the OS from 3+ to 2+ of only one Mn ion (that accepts this extra electron) while all other Mn ions remain unchanged. This process continues when we go on with the Li intercalation until eventually all Mn ions reduce from 3+ to 2+. Thus, these two approaches successfully describe the mixed-valence nature of the Li_xMnPO_4 compound that contains two types of Mn ions, Mn^{3+} and Mn^{2+} , at $x = 1/4, 1/2, 3/4$. In contrast, DFT fails to localize an extra electron on one of the Mn ions and as a consequence the charge density is spread out and equally distributed among all Mn ions in the system with approximately equal occupations, as can be seen in Fig. 3. Hence, in DFT at $x = 1/4, 1/2, 3/4$ there is only one type of Mn ions with the formal oxidation state of 2.5+, which does not make sense since the OS can take only integer values. In the case of Li_xFePO_4 , our results are similar with a difference that here only DFT+ U + V shows the digital change in Löwdin occupations while HSE06 does not manage to describe accurately the localization of electrons on Fe ions in the presence of inter-site hybridizations with O-2 p ligand orbitals. This seems to suggest that the global mixing parameter of 0.25 of HSE06 turns out to be not accurate to describe complex electronic interactions in Li_xFePO_4 , while the site-dependent self-consistent Hubbard U and V parameters are crucial to describe the local chemistry and to find a proper balance between two competing effects, localization of $3d$ electrons and the $3d-2p$ inter-site hybridization. Finally, in $\text{Li}_x\text{Mn}_{1/2}\text{Fe}_{1/2}\text{PO}_4$ we find that Mn^{3+} ions are the first to reduce to Mn^{2+} when lithiating the compound from $x = 0$ to $x = 1/2$, and only then Fe^{3+} ions reduce to Fe^{2+} when further lithiating the compound from $x = 1/2$ to $x = 1$. Importantly, we find that both DFT+ U + V and HSE06 agree to describe the change in the Löwdin occupations on Mn ions, while for Fe ions again we find that DFT+ U + V outpaces HSE06 in terms of accuracy. Similar trends are also observed for magnetic moments for these three materials (see Sec. S5 in SM [82]).

B. Spin-resolved projected density of states

In this section we analyze the spin-resolved PDOS using three levels of theory (DFT, DFT+ U + V , and HSE06). In Fig. S4 we show the spin-resolved PDOS for $\text{Li}_x\text{Mn}_{1/2}\text{Fe}_{1/2}\text{PO}_4$ at different concentrations of Li ($x = 0, 1/4, 1/2, 3/4, 1$) as a representative example of phospho-olivines considered in this paper, while in Sec. S6 in the SM [82] we show the spin-resolved PDOS for Li_xMnPO_4 and Li_xFePO_4 .

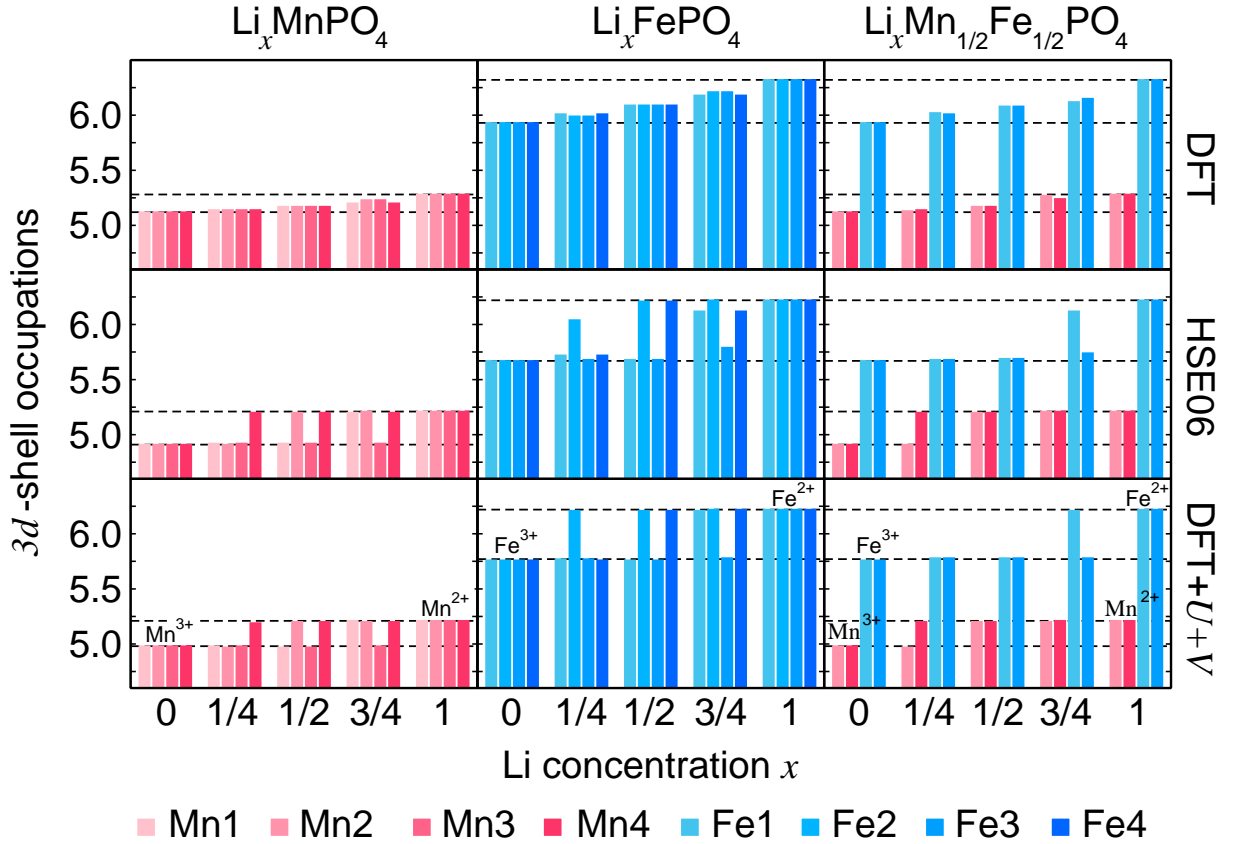


FIG. 3: Löwdin occupations of the $3d$ shell of Mn and Fe atoms in Li_xMnPO_4 , Li_xFePO_4 , and $\text{Li}_x\text{Mn}_{1/2}\text{Fe}_{1/2}\text{PO}_4$ at $x = 0, 1/4, 1/2, 3/4, 1$ computed using three levels of theory (DFT, DFT+ $U+V$, and HSE06). The horizontal dashed lines correspond to the Löwdin occupations of the end elements ($x = 0$ and $x = 1$) with their corresponding oxidation states determined using the data in Table I. For each material there are four TM atoms, each of which is represented with a bar.

We can see from Fig. S4 that overall the PDOS computed using DFT+ $U+V$ and HSE06 agree very well qualitatively, while the PDOS computed using DFT shows significantly different trends. More specifically, due to the overdelocalization of d electrons of TM ions in DFT caused by SIE the Fe- $3d$ and Mn- $3d$ states are grouped around the Fermi level and the material exhibits spurious metallic character at $x = 1/4, 1/2, 3/4$. Furthermore, when increasing the concentration of Li within DFT, there are no clear trends in the changes of PDOS and there is no evidence that only one TM element changes its OS from $3+$ to $2+$ (in agreement with the population analysis of Sec. III A). Instead, the Li-donated extra electron is spread out over all Fe and Mn ions that results in approximately equal PDOS for the likewise TM elements. In contrast, both DFT+ $U+V$ and HSE06 change drastically the PDOS compared to the DFT-based one: the material preserves the insulating character during the whole process of lithiation from $x = 0$ up to $x = 1$ (the reader is referred to Sec. S7 in the SM [82] for the values of band gaps). When changing x from 0 to $1/4$ (i.e. intercalating one Li^+ ion and adding one electron to the

olivine cathode material), only the PDOS of one Mn ion (labeled as “Mn4”) is changing by shifting Mn- $3d$ empty states to higher energies in the spin-up channel and Mn- $3d$ occupied states closer to the top of the valence bands in the spin-down channel. Further by changing x from $1/4$ to $1/2$ the PDOS of the second Mn ion (labeled as “Mn2”) is changing in the same way as the PDOS of Mn4 but mirrored with respect to the spin channels. This is in line with the fact that Mn is the first species to change its occupation when lithiating the structure from $x = 0$ to $x = 1/2$ as shown in Fig. 3. By further lithiating the cathode material from $x = 1/2$ to $3/4$ and finally from $3/4$ to 1 we can see that now the PDOS of the two Fe ions (labeled as “Fe1” and “Fe3”) change by shifting Fe- $3d$ empty states to higher energies and Fe- $3d$ occupied states towards the top of the valence bands. These changes in the PDOS are consistent with the reduction of Mn^{3+} to Mn^{2+} and of Fe^{3+} to Fe^{2+} (see Sec. III A). It is interesting to note that the occupied Fe- $3d$ states are localized and show small hybridization with O- $2p$ ligand states for x in the range from 0 to $1/2$, while they become more delocalized and hybridize stronger with the O- $2p$ states for

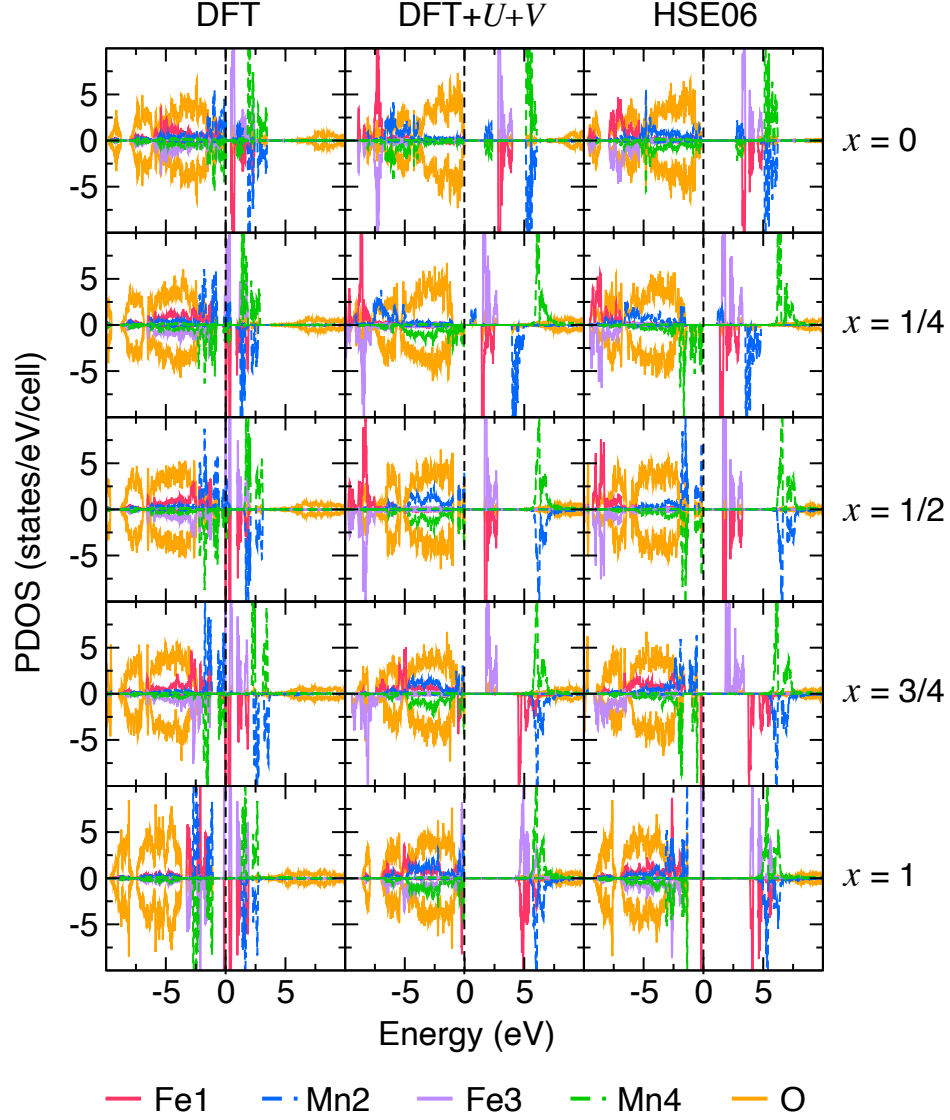


FIG. 4: Spin-resolved PDOS in $\text{Li}_x\text{Mn}_{1/2}\text{Fe}_{1/2}\text{PO}_4$ at different concentrations of Li ($x = 0, 1/4, 1/2, 3/4, 1$) for $3d$ states of Fe1, Mn2, Fe3, Mn4 and for $2p$ states of O, computed using DFT, DFT+ $U+V$, and HSE06. The PDOS for O- $2p$ states was obtained by summing up contributions from all O atoms in the simulation cell and it was multiplied by a factor of 1/2 in order to have clearer comparison with the PDOS of Fe and Mn atoms. The zero of energy corresponds to the top of the valence bands in the case of insulating ground states or the Fermi level in the case of metallic ground states. The upper part of each panel corresponds to the spin-up channel, and the lower part corresponds to the spin-down channel.

x from 1/2 to 1. This latter effect is well captured both in HSE06 and DFT+ $U+V$ since both describe the inter-site electronic interactions and not only the localization of d electrons.

It is instructive to highlight the differences in the PDOS computed using DFT+ $U+V$ and HSE06. While both methods show changes in the character of the top of the valence bands when going from $x = 0$ to 1, the fine

details are different. At $x = 0$, DFT+ U + V shows that the top of the valence bands is strongly dominated by the O-2 p states while HSE06 predicts that the top of the valence bands is more of a mixed nature due to the hybridization between Mn-3 d and O-2 p states. In addition, in DFT+ U + V we can see a clear gap between the Fe-3 d and Mn-3 d empty states at $x = 0$ which is not present in the PDOS from HSE06. At $x = 1/4$ and $x = 1/2$, both methods show that the top of the valence bands is dominated by the Mn-3 d states, although in HSE06 the intensity of these states is much stronger than in DFT+ U + V . Finally, at $x = 3/4$ and 1 these two methods give different predictions for the character of the top of the valence bands. In HSE06 at $x = 1$, Fe-3 d states are the highest occupied states while Mn-3 d states lie deeper in energy and there is an energy gap between these two sets of states. In contrast, in DFT+ U + V at $x = 1$ there is no gap between the Fe-3 d and Mn-3 d occupied states, and all these states overlap in energy and thus the top of the valence bands is predominantly of the Fe-3 d and Mn-3 d character. To the best of our knowledge there is no experimental data from photoemission and X-ray absorption spectroscopy measurements, so it is not possible to establish which method gives a more accurate description of the electronic structure of $\text{Li}_x\text{Mn}_{1/2}\text{Fe}_{1/2}\text{PO}_4$ and other olivines studied here. However, the fact that DFT+ U + V can capture the digital change of Löwdin occupations (especially for Fe ions) upon the lithiation of olivines (as shown in Sec. III A) suggests that probably the PDOS from DFT+ U + V is likely to be more reliable than the one from HSE06. Further investigations are required in order to shed more light on this issue. But the overall agreement between trends in the PDOS computed within DFT+ U + V and HSE06 proves that these two methods - despite having very different mathematical formulations (see Sec. II) - yield on average similar predictions of the electronic structure of phospho-olivines.

C. Lithium intercalation voltages

The intercalation voltages can be computed using the fundamental thermodynamic definition [22, 97]:

$$\Phi = -\frac{E(\text{Li}_{x_2}\text{S}) - E(\text{Li}_{x_1}\text{S}) - (x_2 - x_1)E(\text{Li})}{(x_2 - x_1)e}, \quad (10)$$

where S is introduced for the sake of short-hand notation and it denotes e.g. MnPO_4 for Li_xMnPO_4 and similarly for other cathode materials considered in this paper. Here, Φ is the voltage, e is the electronic charge, x_1 and x_2 are the concentrations of Li and they take values between 0 and 1 in this study, and E is the total energy per formula unit. It is important to remark that $E(\text{Li})$ is the total energy of bulk Li computed at the level of standard DFT (PBEsol functional) while $E(\text{Li}_{x_1}\text{S})$ and $E(\text{Li}_{x_2}\text{S})$ are computed using four levels of theory considered in this work: DFT, HSE06, DFT+ U , and DFT+ U + V (U

and V are computed self-consistently individually for each structure [22]).

Figure 5 shows a comparison of computed voltages with the experimental ones of Refs. [24, 25]. For Li_xMnPO_4 and Li_xFePO_4 we computed the average voltages in the range $0 < x < 1$ (thus $x_1 = 0$ and $x_2 = 1$) since experimentally it is known that there is only one plateau in the voltage profile [25]. In contrast, for $\text{Li}_x\text{Mn}_{1/2}\text{Fe}_{1/2}\text{PO}_4$ we computed the average voltages in two ranges of x , $0 < x < 1/2$ and $1/2 < x < 1$, since experimentally it is known that there are two plateaus in the voltage profile [25]. More specifically, in this latter case $0 < x < 1/2$ corresponds to the reduction of Mn ions and hence the voltage equals to the one of Li_xMnPO_4 , while $1/2 < x < 1$ corresponds to the reduction of Fe ions and hence the voltage equals to the one of Li_xFePO_4 .

As can be seen from Fig. 5, standard DFT largely underestimates the voltages (on average 22 – 31% off with respect to the experiments). This demonstrates that the energetics is strongly affected by the delocalization error of approximate xc functionals (such as e.g. PBEsol) due to strong self-interactions errors for d electrons of TM ions. HSE06 alleviates these errors partially and improves the energetics, however the resulting voltages are overestimated by 6 – 15%. DFT+ U shown different trends with respect to HSE06 voltages depending on the material and the range of x : it gives somewhat higher voltages than HSE06 for Li_xMnPO_4 , but it gives lower voltages than HSE06 for Li_xFePO_4 (and it gets closer to the experimental value). Thus, the percentage of the deviation of DFT+ U voltages from the experimental ones are slightly more scattered than the HSE06 ones and are 3 – 14%. It is useful to remark that our DFT+ U voltages for Li_xMnPO_4 and Li_xFePO_4 are in much closer agreement with the experimental ones than those of Ref. [22]; as was pointed out in Ref. [21], this is a consequence of the difference in the values of U , and of the consistent calculation of forces and stresses using the orthogonalized atomic Hubbard projectors [see Eq. (7)] that has significantly refined the prediction of the equilibrium crystal structure in this work. Finally, DFT+ U + V gives the most accurate predictions of voltages compared to all other methods considered in this work. More specifically, the average deviation of DFT+ U + V voltages from the experimental ones is 1 – 7%; leaving aside the $\text{Li}_x\text{Mn}_{1/2}\text{Fe}_{1/2}\text{PO}_4$ case with $1/2 < x < 1$, the average deviation is 1 – 2% which is remarkable given the fact that the DFT+ U + V calculations are fully first-principles with no fitting or adjustment parameters. This finding demonstrates that the accuracy of the DFT+ U + V approach with U and V computed using linear-response theory [19, 45] in a self-consistent fashion [21, 22] is satisfactory for predictive simulations of olivine-type cathode materials. These promising results and observations motivate investigations of other classes of cathode materials using extended Hubbard functionals, and the work is in progress in this direction.

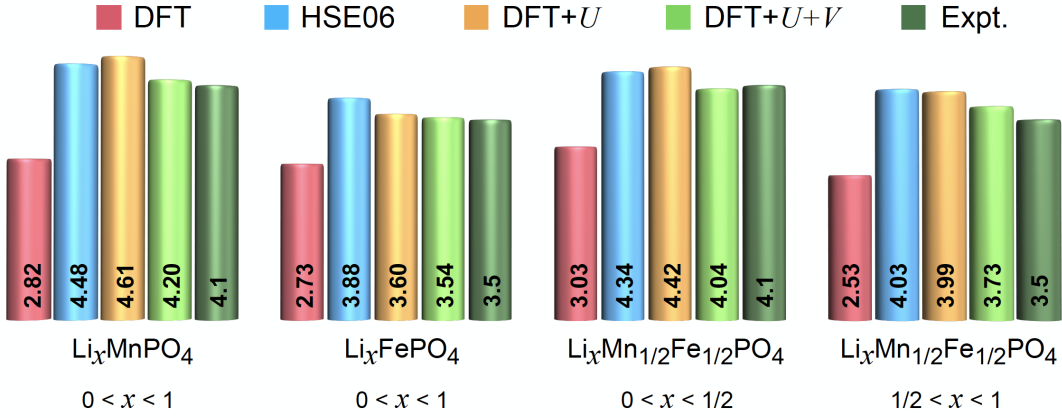


FIG. 5: Voltages vs. Li/Li^+ (in V) for Li_xMnPO_4 , Li_xFePO_4 , and $\text{Li}_x\text{Mn}_{1/2}\text{Fe}_{1/2}\text{PO}_4$ computed using DFT, HSE06, DFT+U, and DFT+U+V with U and V determined from first-principles. The experimental data is from Refs. [24, 25].

IV. CONCLUSIONS

We have presented the first comparative study (DFT, DFT+U, DFT+U+V, and HSE06) of the electronic properties and the energetics of lithium intercalation in representative phospho-olivine cathode materials: Li_xMnPO_4 , Li_xFePO_4 , and $\text{Li}_x\text{Mn}_{1/2}\text{Fe}_{1/2}\text{PO}_4$ ($x = 0, 1/4, 1/2, 3/4, 1$). In DFT+U and DFT+U+V, the Hubbard parameters U and V have been computed from first principles using density-functional perturbation theory, without any need for adjustments or *ad hoc* fitting of the model.

By determining the oxidation state of TM ions *via* the Löwdin occupations of their d manifolds, we were able to analyse their change during the lithiation process. We have found that DFT fails to account for the onset of disproportionation of the TM atoms along the intermediates of the lithiation process. In contrast, DFT+U+V correctly predicts the digital change of Löwdin occupations upon Li intercalation (only one TM ions changes its oxidation state from 3+ to 2+ when adding one Li ion) in all materials studied here. For comparison, HSE06 shows the digital change in occupations for Li_xMnPO_4 but it fails to do so for Li_xFePO_4 at $x = 1/4$ and $3/4$ and for $\text{Li}_x\text{Mn}_{1/2}\text{Fe}_{1/2}\text{PO}_4$ at $x = 3/4$. Furthermore, the investigation of the electronic structure has revealed that both DFT+U+V and HSE06 qualitatively show similar trends

in the spin-resolved projected density of states, while DFT fails dramatically due to strong self-interactions errors.

Finally, the computed intercalation voltages are greatly underestimated within DFT, whereas HSE06 brings voltages closer to the experimental values, albeit overestimating them. On the other hand, while DFT+U is in general only slightly worse than HSE06, DFT+U+V overcomes this limitation and actually outperforms HSE06 in terms of accuracy, producing voltages in very good agreement with experiments. These findings motivate the investigation of the electrochemical properties of other classes of cathode materials (e.g. layered, spinel, etc.) using DFT+U+V, and work is underway along these paths. Finally, this study opens the way for a reliable and fully first-principles design and characterization of novel cathode materials with affordable computational cost and high level of accuracy.

ACKNOWLEDGEMENTS

We acknowledge support by the Swiss National Science Foundation (SNSF), through grant 200021-179138, and its National Centre of Competence in Research (NCCR) MARVEL. F.A. acknowledges the European H2020 Intersect project, Grant No. 814487. Computer time was provided by the Swiss National Supercomputing Centre (CSCS) under project No. s1073.

-
- [1] J. Goodenough and K.-S. Park, The Li-Ion Rechargeable Battery: A Perspective, *J. Am. Chem. Soc.* **135**, 1167 (2013).
 - [2] G. Assat and J. Tarascon, Fundamental understanding and practical challenges of anionic redox activity in Li-ion batteries, *Nat. Ener.* **3**, 373 (2018).

- [3] D. Larcher and J. Tarascon, Towards greener and more sustainable batteries for electrochemical energy storage, *Nat. Chem.* **7**, 19 (2014).
- [4] B. Kang and G. Ceder, Battery materials for ultrafast charging and discharging, *Nature* **458**, 190 (2009).

- [5] L. Monconduit, L. Croguennec, and R. Dedryvère, *Electrodes for Li-ion Batteries*, Vol. 2nd (Wiley, London, 2015).
- [6] J. Lee, A. Urban, X. Li, D. Su, G. Hautier, and G. Ceder, Unlocking the Potential of Cation-Disordered Oxides for Rechargeable Lithium Batteries, *Science* **343**, 519 (2014).
- [7] K. Hurlbutt, S. Wheeler, I. Capone, and M. Pasta, Prussian Blue Analogues as Cathode Materials, *Joule* **2**, 1950 (2018).
- [8] P. Hohenberg and W. Kohn, Inhomogeneous electron gas, *Phys. Rev.* **136**, B864 (1964).
- [9] W. Kohn and L. Sham, Self-consistent equations including exchange and correlation effects, *Phys. Rev.* **140**, A1133 (1965).
- [10] J. Perdew and A. Zunger, Self-interaction correction to density-functional approximations for many-electron systems, *Phys. Rev. B* **23**, 5048 (1981).
- [11] P. Mori-Sánchez, A. Cohen, and W. Yang, Many-electron self-interaction error in approximate density functionals, *J. Chem. Phys.* **125**, 201102 (2006).
- [12] V. Anisimov, J. Zaanen, and O. Andersen, Band theory and Mott insulators: Hubbard U instead of Stoner I , *Phys. Rev. B* **44**, 943 (1991).
- [13] A. Liechtenstein, V. Anisimov, and J. Zaanen, Density-functional theory and strong interactions: Orbital ordering in Mott-Hubbard insulators, *Phys. Rev. B* **52**, R5467 (1995).
- [14] S. Dudarev, G. Botton, S. Savrasov, C. Humphreys, and A. Sutton, Electron-energy-loss spectra and the structural stability of nickel oxide: An LSDA+ U study, *Physical Review B* **57**, 1505 (1998).
- [15] V. L. Campo Jr and M. Cococcioni, Extended DFT+ U + V method with on-site and inter-site electronic interactions, *J. Phys.: Condens. Matter* **22**, 055602 (2010).
- [16] N. Tancogne-Dejean and A. Rubio, Parameter-free hybridlike functional based on an extended Hubbard model: DFT+ U + V , *Phys. Rev. B* **102**, 155117 (2020).
- [17] S.-H. Lee and Y.-W. Son, First-principles approach with a pseudohybrid density functional for extended Hubbard interactions, *Phys. Rev. Research* **2**, 043410 (2020).
- [18] C. Adamo and V. Barone, Toward reliable density functional methods without adjustable parameters: The PBE0 model, *J. Chem. Phys.* **110**, 6158 (1999).
- [19] J. Heyd, G. Scuseria, and M. Ernzerhof, Hybrid functionals based on a screened Coulomb potential, *J. Chem. Phys.* **118**, 8207 (2003).
- [20] J. Heyd, G. Scuseria, and M. Ernzerhof, Erratum: "Hybrid functionals based on a screened Coulomb potential" [*J. Chem. Phys.* **118**, 8207 (2003)], *J. Chem. Phys.* **124**, 219906 (2006).
- [21] J. Sun, A. Ruzsinszky, and J. Perdew, Strongly Constrained and Appropriately Normed Semilocal Density Functional, *Phys. Rev. Lett.* **115**, 036402 (2015).
- [22] A. Bartók and J. Yates, Regularized SCAN functional, *J. Chem. Phys.* **150**, 161101 (2019).
- [23] J. Furness, A. Kaplan, J. Ning, J. Perdew, and J. Sun, Accurate and Numerically Efficient r^2 SCAN Meta-Generalized Gradient Approximation, *J. Phys. Chem. Lett.* **11**, 8208 (2020).
- [24] H. Kulik and N. Marzari, A self-consistent Hubbard U density-functional theory approach to the addition-elimination reactions of hydrocarbons on bare FeO^+ , *J. Chem. Phys.* **129**, 134314 (2008).
- [25] Meta-GGA functional SCAN has gained a lot of interest since its creation in 2015, in particular for modeling of cathode materials. Recent application of SCAN has shown that it gives improved description of electronic properties and voltages in layered cathode materials [98], however SCAN does not eliminate the need of the Hubbard U correction in olivine and spinel materials [99]. In addition, it is important to note that despite being very successful for a broad class of materials and properties, SCAN still contains significant SIE especially when applied to TM compounds [100, 101], it exhibits some potential limitations in describing magnetic systems [102, 103], and from a technical point of view currently there are only few SCAN-based pseudopotentials (PPs) [104] and often GGA-based PP are used that is known to introduce noticeable errors in calculating some properties of materials as e.g. phase transition energies [105].
- [26] B. Himmetoglu, A. Floris, S. de Gironcoli, and M. Cococcioni, Hubbard-corrected DFT energy functionals: The LDA+ U description of correlated systems, *Int. J. Quant. Chem.* **114**, 14 (2014).
- [27] The actual values produced by each of first-principles approaches for determining U and V may vary substantially, in addition to the intrinsic dependence on the choice of the projector functions for the Hubbard manifold, pseudopotentials, oxidation state, functional, etc.
- [28] P. Dederichs, S. Blügel, R. Zeller, and H. Akai, Ground States of Constrained Systems: Application to Cerium Impurities, *Phys. Rev. Lett.* **53**, 2512 (1984).
- [29] A. McMahan, R. Martin, and S. Satpathy, Calculated effective Hamiltonian for La_2CuO_4 and solution in the impurity Anderson approximation, *Phys. Rev. B* **38**, 6650 (1988).
- [30] O. Gunnarsson, O. Andersen, O. Jepsen, and J. Zaanen, Density-functional calculation of the parameters in the Anderson model: Application to Mn in CdTe, *Phys. Rev. B* **39**, 1708 (1989).
- [31] M. Hybertsen, M. Schlüter, and N. Christensen, Calculation of Coulomb-interaction parameters for La_2CuO_4 using a constrained-density-functional approach, *Phys. Rev. B* **39**, 9028 (1989).
- [32] O. Gunnarsson, Calculation of parameters in model Hamiltonians, *Phys. Rev. B* **41**, 514 (1990).
- [33] W. Pickett, S. Erwin, and E. Ethridge, Reformulation of the LDA+ U method for a local-orbital basis, *Phys. Rev. B* **58**, 1201 (1998).
- [34] I. Solovyev and M. Imada, Screening of Coulomb interactions in transition metals, *Phys. Rev. B* **71**, 045103 (2005).
- [35] K. Nakamura, R. Arita, Y. Yoshimoto, and S. Tsuneyuki, First-principles calculation of effective onsite Coulomb interactions of $3d$ transition metals: Constrained local density functional approach with maximally localized Wannier functions, *Phys. Rev. B* **74**, 235113 (2006).
- [36] M. Shishkin and H. Sato, Self-consistent parametrization of DFT+ U framework using linear response approach: Application to evaluation of redox potentials of battery cathodes, *Phys. Rev. B* **93**, 085135 (2016).
- [37] N. Mosey and E. Carter, Ab initio evaluation of Coulomb and exchange parameters for DFT+ U calculations, *Phys. Rev. B* **76**, 155123 (2007).
- [38] N. Mosey, P. Liao, and E. Carter, Rotationally invariant ab initio evaluation of Coulomb and exchange parameters

- for DFT+U calculations, J. Chem. Phys. **129**, 014103 (2008).
- [39] A. Andriotis, R. Sheetz, and M. Menon, LSDA+ U method: A calculation of the U values at the Hartree-Fock level of approximation, Phys. Rev. B **81**, 245103 (2010).
- [40] L. Agapito, S. Curtarolo, and M. Buongiorno Nardelli, Reformulation of DFT+ U as a Pseudohybrid Hubbard Density Functional for Accelerated Materials Discovery, Phys. Rev. X **5**, 011006 (2015).
- [41] M. Springer and F. Aryasetiawan, Frequency-dependent screened interaction in Ni within the random-phase approximation, Phys. Rev. B **57**, 4364 (1998).
- [42] T. Kotani, *Ab initio* random-phase-approximation calculation of the frequency-dependent effective interaction between 3d electrons: Ni, Fe, and MnO, J. Phys.: Condens. Matter **12**, 2413 (2000).
- [43] F. Aryasetiawan, M. Imada, A. Georges, G. Kotliar, S. Biermann, and A. Lichtenstein, Frequency-dependent local interactions and low-energy effective models from electronic structure calculations, Phys. Rev. B **70**, 195104 (2004).
- [44] F. Aryasetiawan, K. Karlsson, O. Jepsen, and U. Schönberger, Calculations of Hubbard U from first-principles, Phys. Rev. B **74**, 125106 (2006).
- [45] M. Cococcioni and S. de Gironcoli, Linear response approach to the calculation of the effective interaction parameters in the LDA+ U method, Phys. Rev. B **71**, 035105 (2005).
- [19] I. Timrov, N. Marzari, and M. Cococcioni, Hubbard parameters from density-functional perturbation theory, Phys. Rev. B **98**, 085127 (2018).
- [21] I. Timrov, N. Marzari, and M. Cococcioni, Self-consistent Hubbard parameters from density-functional perturbation theory in the ultrasoft and projector-augmented wave formulations, Phys. Rev. B **103**, 045141 (2021).
- [48] F. Zhou, C. Marianetti, M. Cococcioni, D. Morgan, and G. Ceder, Phase separation in LiFePO₄ induced by correlation effects, Phys. Rev. B **69**, 201101(R) (2004).
- [49] F. Zhou, M. Cococcioni, C. Marianetti, D. Morgan, and G. Ceder, First-principles prediction of redox potentials in transition-metal compounds with LDA+ U , Phys. Rev. B **70**, 235121 (2004).
- [50] F. Zhou, K. Kang, T. Maxisch, G. Ceder, and D. Morgan, The electronic structure and band gap of LiFePO₄ and LiMnPO₄, Solid State Commun. **132**, 181 (2004).
- [51] B. Kim, K. Kim, and S. Kim, Quantification of Coulomb interactions in layered lithium and sodium battery cathode materials, Phys. Rev. Materials **5**, 035404 (2021).
- [22] M. Cococcioni and N. Marzari, Energetics and cathode voltages of LiMPO₄ olivines (M =Fe, Mn) from extended Hubbard functionals, Phys. Rev. Materials **3**, 033801 (2019).
- [53] J. Skone, M. Govoni, and G. Galli, Self-consistent hybrid functional for condensed systems, Phys. Rev. B **89**, 195112 (2014).
- [54] J. Skone, M. Govoni, and G. Galli, Nonempirical range-separated hybrid functionals for solids and molecules, Phys. Rev. B **93**, 235106 (2016).
- [55] T. Bischoff, J. Wiktor, W. Chen, and A. Pasquarello, Nonempirical hybrid functionals for band gaps of inorganic metal-halide perovskites, Phys. Rev. Mater. **3**, 123802 (2019).
- [56] L. Kronik, T. Stein, S. Refaely-Abramson, and R. Baer, Excitation gaps of finite-sized systems from optimally tuned range-separated hybrid functionals, J. Chem. Theory Comput. **8**, 1515 (2012).
- [57] D. Wing, G. Ohad, J. Haber, M. Filip, S. Gant, J. Neaton, and L. Kronik, Band gaps of crystalline solids from Wannier-localization based optimal tuning of a screened range-separated hybrid functional, arXiv:2012.03278 [cond-mat.mtrl-sci] (2020).
- [58] M. Lorke, P. Deák, and T. Frauenheim, Koopmans-compliant screened exchange potential with correct asymptotic behavior for semiconductors, Phys. Rev. B **102**, 235168 (2020).
- [59] S. Ong, V. Chevrier, and G. Ceder, Comparison of small polaron migration and phase separation in olivine LiMnPO₄ and LiFePO₄ using hybrid density functional theory, Phys. Rev. B **83**, 075112 (2011).
- [60] M. Eckhoff, P. Blöchl, and J. Behler, Hybrid density functional theory benchmark study on lithium manganese oxides, Phys. Rev. B **101**, 205113 (2020).
- [61] E. Linscott, D. Cole, M. Payne, and D. O'Regan, Phys. Rev. B **98**, 235157 (2018).
- [62] C. Tablero, Representations of the occupation number matrix on the LDA/GGA+ U method, J. Phys.: Condens. Matter **20**, 325205 (2008).
- [63] Y.-C. Wang, Z.-H. Chen, and H. Jiang, The local projection in the density functional theory plus U approach: A critical assessment, J. Chem. Phys. **144**, 144106 (2016).
- [13] I. Timrov, F. Aquilante, L. Binci, M. Cococcioni, and N. Marzari, Pulay forces in density-functional theory with extended Hubbard functionals: from nonorthogonalized to orthogonalized manifolds, Phys. Rev. B **102**, 235159 (2020).
- [11] P.-O. Löwdin, On the Non-Orthogonality Problem Connected with the Use of Atomic Wave Functions in the Theory of Molecules and Crystals, J. Chem. Phys. **18**, 365 (1950).
- [12] I. Mayer, On Löwdin's method of symmetric orthogonalization, Int. J. Quant. Chem. **90**, 63 (2002).
- [67] C. Ricca, I. Timrov, M. Cococcioni, N. Marzari, and U. Aschauer, Self-consistent DFT+ U + V study of oxygen vacancies in SrTiO₃, Phys. Rev. Research **2**, 023313 (2020).
- [68] I. Timrov, P. Agrawal, X. Zhang, S. Erat, R. Liu, A. Braun, M. Cococcioni, M. Calandra, N. Marzari, and D. Passerone, Electronic structure of Ni-substituted LaFeO₃ from near edge x-ray absorption fine structure experiments and first-principles simulations, Phys. Rev. Research **2**, 033265 (2020).
- [69] N. Kirchner-Hall, W. Zhao, Y. Xiong, I. Timrov, and I. Dabo, Extensive Benchmarking of DFT+ U Calculations for Predicting Band Gaps, Appl. Sci. **11**, 2395 (2021).
- [70] Y. Xiong, Q. Campbell, J. Fanghanel, C. Badding, H. Wang, N. Kirchner-Hall, M. Theibault, I. Timrov, J. Mondschein, K. Seth, R. Katz, A. Molina Villarino, B. Pamuk, M. Penrod, M. Khan, T. Rivera, N. Smith, X. Quintana, P. Orbe, C. Fennie, S. Asem-Hiablie, J. Young, T. Deutsch, M. Cococcioni, V. Gopalan, H. Abruña, R. Schaak, and I. Dabo, Optimizing accuracy and efficacy in data-driven materials discovery for the solar production of hydrogen, Energy Environ. Sci. **14**, 2335 (2021).

- [71] M. Cococcioni and A. Floris, Magnetic Energy Landscape of Dimolybdenum Tetraacetate on a Bulk Insulator Surface, *Appl. Sci.* **11**, 3806 (2021).
- [72] R. Mahajan, I. Timrov, N. Marzari, and A. Kashyap, Importance of intersite Hubbard interactions in β - MnO_2 : A first-principles DFT+ U + V study, *Phys. Rev. Materials* **5**, 104402 (2021).
- [73] T. Kotani, Exact exchange potential band-structure calculations by the linear muffin-tin orbital-atomic-sphere approximation method, *Phys. Rev. Lett.* **74**, 2989 (1995).
- [74] In Refs. [106, 107] a connection between DFT+ U and GW [108] was established. Also, there were studies trying to understand whether DFT+ U mimics hybrid functionals [109–112], with the conclusion saying that it may or may not mimic hybrids depending on the atom, the subshell, and the property which is considered.
- [23] Z. Nie, C. Ouyang, J. Chen, Z. Zhong, Y. Du, D. Liu, S. Shi, and M. Lei, First principles study of Jahn-Teller effects in Li_xMnPO_4 , *Solid State Commun.* **150**, 40 (2010).
- [24] A. Padhi, K. Nanjundaswamy, and J. Goodenough, Phospho-olivines as Positive-Electrode Materials for Rechargeable Lithium Batteries, *J. Electrochem. Soc.* **144**, 1188 (1997).
- [25] T. Muraliganth and A. Manthiram, Understanding the Shifts in the Redox Potentials of Olivines $\text{LiM}_{1-y}\text{M}_y\text{PO}_4$ ($M = \text{Fe, Mn, Co, and Mg}$) Solid Solution Cathodes, *J. Phys. Chem. C* **114**, 15530 (2010).
- [28] R. Newnham, R. Santoro, and M. Redman, Neutron-diffraction study of LiMnPO_4 , *J. Phys. Chem. Solids* **26**, 445 (1965).
- [79] R. Santoro and R. Newnham, Antiferromagnetism in LiFePO_4 , *Acta Cryst.* **22**, 344 (1967).
- [29] G. Rousse, J. Rodriguez-Carvajal, S. Patoux, and C. Masquelier, Magnetic Structures of the Triphylite LiFePO_4 and of Its Delithiated Form FePO_4 , *Chem. Mater.* **15**, 4082 (2003).
- [27] S. Gnewuch and E. Rodriguez, Distinguishing the Intrinsic Antiferromagnetism in Polycrystalline LiCoPO_4 and LiMnPO_4 Olivines, *Inorg. Chem.* **59**, 5883 (2020).
- [82] Supplemental Material is included in this PDF file (see after page 15).
- [26] P. H.-L. Sit, R. Car, M. H. Cohen, and A. Selloni, Simple, Unambiguous Theoretical Approach to Oxidation State Determination via First-Principles Calculations, *Inorg. Chem.* **50**, 10259 (2011).
- [84] C. Jorgensen, *Oxidation Numbers and Oxidation States* (Springer-Verlag, New York Inc., 1969).
- [85] <https://goldbook.iupac.org/O04365.html>.
- [86] R. Bader, *Atoms in Molecules. A Quantum Theory* (Oxford University Press, Oxford, U.K., 1990).
- [87] F. Bickelhaupt, N. van Eikema, C. Fonseca Guerra, and E. Baerends, The Carbon-Lithium Electron Pair Bond in $(\text{CH}_3\text{Li})_n$ ($n = 1, 2, 4$), *Organometallics* **15**, 2923 (1996).
- [88] R. Mulliken, Electronic Population Analysis on LCAO–MO Molecular Wave Functions. I, *J. Chem. Phys.* **23**, 1833 (1955).
- [89] A. Reed, L. Curtiss, and F. Weinhold, Intermolecular interactions from a natural bond orbital, donor-acceptor viewpoint, *Chem. Rev.* **88**, 899 (1988).
- [90] H. Raebiger, S. Lany, and A. Zunger, Charge self-regulation upon changing the oxidation state of transition metals in insulators, *Nature* **453**, 763 (2008).
- [91] R. Resta, Charge states in transition, *Nature* **453**, 735 (2008).
- [92] Jansen, M. and Wedig, U., A Piece of the Picture - Misunderstanding of Chemical Concepts, *Angew. Chem., Int. Ed.* **47**, 10026 (2008).
- [93] L. Jiang, S. Levchenko, and A. Rappe, Rigorous Definition of Oxidation States of Ions in Solids, *Phys. Rev. Lett.* **108**, 166403 (2012).
- [94] P. Pegolo, F. Grasselli, and S. Baroni, Oxidation States, Thouless' Pumps, and Nontrivial Ionic Transport in Nonstoichiometric Electrolytes, *Phys. Rev. X* **10**, 041031 (2020).
- [95] Possible reasons of deviations of eigenvalues (corresponding to the fully occupied states) from unity is discussed in Ref. [26].
- [96] O. Ofer, J. Sugiyama, J. Brewer, M. Månsson, K. Prša, E. Ansaldi, G. Kobayashi, and R. Kanno, The magnetic phase of Lithium transition metal phosphates LiMPO_4 ($M = \text{Mn, Co, Ni}$) detected by μ^+ SR, *Physics Procedia* **30**, 160 (2012).
- [97] M. Aydinol, A. Kohan, G. Ceder, K. Cho, and J. Joannopoulos, *Ab initio* study of lithium intercalation in metal oxides and metal dichalcogenides, *Phys. Rev. B* **56**, 1354 (1997).
- [98] A. Chakraborty, M. Dixit, D. Aurbach, and D. Major, Predicting accurate cathode properties of layered oxide materials using the SCAN meta-GGA density functional, *npj Comput. Mater.* **4**, 60 (2018).
- [99] E. Isaacs, S. Patel, and C. Wolverton, Prediction of Li intercalation voltages in rechargeable battery cathode materials: Effects of exchange-correlation functional, van der Waals interactions, and Hubbard U , *Phys. Rev. Materials* **4**, 065405 (2020).
- [100] D. A. Kitchaev, H. Peng, Y. Liu, J. Sun, J. P. Perdew, and G. Ceder, Energetics of MnO_2 polymorphs in density functional theory, *Physical Review B* **93**, 045132 (2016).
- [101] Y. Hinuma, H. Hayashi, Y. Kumagai, I. Tanaka, and F. Oba, Comparison of approximations in density functional theory calculations: Energetics and structure of binary oxides, *Phys. Rev. B* **96**, 094102 (2017).
- [102] M. Ekholm, D. Gambino, H. Jönsson, F. Tasnádi, B. Alling, and I. Abrikosov, Assessing the SCAN functional for itinerant electron ferromagnets, *Phys. Rev. B* **98**, 094413 (2018).
- [103] F. Tran, G. Baudesson, J. Carrete, G. Madsen, P. Blaha, K. Schwarz, and D. Singh, Shortcomings of meta-GGA functionals when describing magnetism, *Phys. Rev. B* **102**, 024407 (2020).
- [104] <https://yaoyi92.github.io/scan-tm-pseudopotentials.html>.
- [105] Y. Yao and Y. Kanai, Plane-wave pseudopotential implementation and performance of SCAN meta-GGA exchange-correlation functional for extended systems, *J. Chem. Phys.* **146**, 224105 (2017).
- [106] V. Anisimov, F. Aryasetiawan, and A. Lichtenstein, First-principles calculations of the electronic structure and spectra of strongly correlated systems: the LDA+ U method, *J. Phys.: Condens. Matter* **9**, 767 (1997).
- [107] H. Jiang, R. Gomez-Abal, P. Rinke, and M. Scheffler, First-principles modeling of localized d states with the $GW@LDA+U$ approach, *Phys. Rev. B* **82**, 045108 (2010).
- [108] L. Hedin, New Method for Calculating the One-Particle Green's Function with Application to the Electron-Gas

- Problem, Phys. Rev. **139**, A796 (1965).
- [109] V. Iváady, R. Armiento, K. Szász, E. Janzén, A. Gali, and I. Abrikosov, Theoretical unification of hybrid-DFT and DFT+ U methods for the treatment of localized orbitals, Phys. Rev. B **90**, 035146 (2014).
 - [110] P. Verma and D. Truhlar, Does DFT+ U mimic hybrid density functionals?, Theor. Chem. Ac. **135**, 182 (2016).
 - [111] T. Gani and H. Kulik, Where Does the Density Localize? Convergent Behavior for Global Hybrids, Range Separation, and DFT+ U , J. Chem. Theor. Comput. **12**, 5931 (2016).
 - [112] Q. Zhao and H. Kulik, Where Does the Density Localize in the Solid State? Divergent Behavior for Hybrids and DFT+ U , J. Chem. Theor. Comput. **14**, 670 (2018).

Supplemental Material for

“Accurate electronic properties and intercalation voltages of olivine-type Li-ion cathode materials from extended Hubbard functionals”

Iurii Timrov, Francesco Aquilante, Matteo Cococcioni, and Nicola Marzari

S1. Technical details

All calculations were performed using the plane-wave (PW) pseudopotential method as implemented in the QUANTUM ESPRESSO distribution [1–3].

We have used the exchange-correlation functional constructed using σ -GGA with the PBEsol prescription [4]. For DFT, DFT+ U , and DFT+ U + V calculations we have used pseudopotentials (PPs) from the SSPP library v1.1 (precision) [5, 6], which are either ultrasoft (US) or projector-augmented-wave (PAW): For manganese we have used `mn_pbesol_v1.5.uspp.F.UPF` from the GBRV v1.5 library [7], for iron and oxygen `Fe.pbesol-spn-kjpaw_psl.0.2.1.UPF` and `O.pbesol-n-kjpaw_psl.0.1.1.UPF` from the Pslibrary v0.3.1 [8], and for phosphorus `P.pbesol-n-rrkjus_psl.1.1.0.0.UPF` from the Pslibrary v1.0.0 [9]. For HSE06 calculations we have used norm-conserving PPs from the PSEUDOJOJO library [10].

To construct the Hubbard projector functions $\varphi_m^I(\mathbf{r})$ [see Eq. (9) in the main text] we have used atomic orbitals which are orthogonalized using Löwdin’s method [11, 12]. Structural optimizations using DFT+ U and DFT+ U + V are performed using orthogonalized atomic orbitals as described in detail in Ref. [13]. The Brillouin zone was sampled using the uniform Γ -centered \mathbf{k} point mesh of size $5 \times 8 \times 9$. Kohn-Sham (KS) wavefunctions and potentials are expanded in PWs up to a kinetic-energy cutoff of 90 and 1080 Ry, respectively, for structural optimization. The crystal structure was optimized using the Broyden-Fletcher-Goldfarb-Shanno (BFGS) algorithm [14], with a convergence threshold for the total energy of 10^{-6} Ry, for forces of 10^{-5} Ry/Bohr, and for pressure of 0.5 Kbar. For the metallic ground states (that appear at the DFT level of theory and intermediate Li concentrations), we have used the Marzari-Vanderbilt smearing method [15] with a broadening parameter of 0.01 Ry.

The DFPT calculations of Hubbard parameters are performed using the HP code [16] of QUANTUM ESPRESSO using the uniform Γ -centered \mathbf{k} and \mathbf{q} point meshes of size $3 \times 4 \times 5$ and $1 \times 2 \times 3$, respectively, which give an accuracy of 0.01 eV for the computed values of U and V . The KS wavefunctions and potentials are expanded in PWs up to a kinetic-energy cutoff of 65 and 780 Ry, respectively, for calculation of Hubbard parameters. The linear-response KS equations of DFPT are solved using the conjugate-gradient algorithm [17] and the mixing scheme of Ref. [18] for the response potential to speed up convergence.

The HSE06 calculations are performed using the uniform Γ -centered \mathbf{k} and \mathbf{q} point meshes of size $6 \times 8 \times 10$ and $3 \times 4 \times 5$, respectively. We recall here that the meaning of the \mathbf{q} point mesh has a different meaning in HSE06 and in DFPT: in the former case, the \mathbf{q} mesh has the same meaning as the \mathbf{k} mesh but it is used to reduce the computational cost of the HSE06 calculations, while in the latter case the \mathbf{q} points represent different monochromatic perturbations that have different modulation [19]. The $\mathbf{q} \rightarrow 0$ limit in HSE06 was treated using the Gygi-Baldereschi scheme [20]. The KS wavefunctions and potentials are expanded in PWs up to a kinetic-energy cutoff of 80 and 320 Ry, respectively, while the exact-exchange (Fock) term was expanded in PWs up to 80 Ry.

The spin-resolved projected density of states (PDOS) at all levels of theory was computed using a Γ -centered \mathbf{k} point mesh of size $6 \times 8 \times 10$, with the Gaussian smearing and a broadening parameter of 10^{-3} Ry.

S2. Hubbard parameters

Table S1 contains the values of onsite U and intersite V Hubbard parameters for Mn(3d) and Fe(3d) states in phospho-olivines considered here, which were computed in the framework of DFT+ U + V self-consistently using DFPT [19, 21] with orthogonalized atomic orbitals as Hubbard projectors, as described in Sec. II.C of the main text. We have also computed the onsite Hubbard U in the framework of DFT+ U – these values are smaller than U ’s reported in Table S1 due to differences in the electronic screening [22]. More specifically, within DFT+ U for Li_xMnPO_4 we obtain $U(\text{Mn})=6.19$ eV for $x=0$ and $U(\text{Mn})=4.30$ eV for $x=1$; for Li_xFePO_4 , Hubbard $U(\text{Fe})=5.00$ eV for $x=0$ and $U(\text{Fe})=4.99$ eV for $x=1$; and, for $\text{Li}_x\text{Mn}_{1/2}\text{Fe}_{1/2}\text{PO}_4$, $U(\text{Fe})=5.01$ eV and $U(\text{Mn})=6.23$ eV for $x=0$, and $U(\text{Fe})=4.97$ eV and $U(\text{Mn})=4.32$ eV for $x=1$.

From Table S1 we can see how the values of Hubbard parameters change upon a lithiation of the phospho-olivines. The general trend when going from $x=0$ to $x=1$ is that the values of Hubbard parameters decrease. Namely, Hubbard U decreases because the 3d manifolds of TM ions acquire an extra electron due to the insertion of Li; the more electrons there is in the Hubbard manifold, the weaker is the screened Coulomb interaction between them, and

Material	x	HP	Mn1	Mn2	Mn3	Mn4
Li_xMnPO_4	0	U	6.26	6.26	6.26	6.26
		V	0.54-1.07	0.54-1.07	0.54-1.07	0.54-1.07
	1/4	U	6.26	6.25	6.67	5.44
		V	0.40-1.01	0.46-1.05	0.54-1.11	0.39-1.08
	1/2	U	6.42	4.95	6.41	4.94
		V	0.34-1.01	0.38-0.96	0.34-1.01	0.38-0.96
	3/4	U	4.67	4.64	6.58	4.98
		V	0.48-0.72	0.31-0.91	0.33-1.02	0.41-0.79
	1	U	4.56	4.56	4.56	4.56
		V	0.42-0.78	0.42-0.78	0.42-0.78	0.42-0.78
Material	x	HP	Fe1	Fe2	Fe3	Fe4
Li_xFePO_4	0	U	5.43	5.43	5.43	5.43
		V	0.60-1.08	0.60-1.08	0.60-1.08	0.60-1.08
	1/4	U	5.39	5.74	5.44	5.40
		V	0.53-1.01	0.50-1.21	0.61-1.09	0.44-0.96
	1/2	U	5.37	5.58	5.37	5.58
		V	0.48-0.92	0.43-0.93	0.48-0.92	0.43-0.93
	3/4	U	5.65	5.41	5.38	5.31
		V	0.49-1.01	0.30-0.99	0.48-0.93	0.39-0.88
	1	U	5.29	5.29	5.29	5.29
		V	0.42-0.90	0.42-0.90	0.42-0.90	0.42-0.90
Material	x	HP	Fe1	Fe3	Mn2	Mn4
$\text{Li}_x\text{Mn}_{1/2}\text{Fe}_{1/2}\text{PO}_4$	0	U	5.43	5.43	6.27	6.27
		V	0.60-1.12	0.60-1.12	0.55-1.05	0.55-1.05
	1/4	U	5.50	5.40	6.24	5.01
		V	0.51-1.12	0.60-1.11	0.43-1.00	0.35-0.96
	1/2	U	5.44	5.44	4.81	4.81
		V	0.54-1.06	0.54-1.06	0.28-0.91	0.28-0.91
	3/4	U	5.59	5.42	4.79	4.59
		V	0.48-0.93	0.48-0.94	0.33-0.91	0.41-0.76
	1	U	5.28	5.28	4.58	4.58
		V	0.41-0.89	0.41-0.89	0.42-0.80	0.42-0.80

TABLE S1: Self-consistent Hubbard parameters (HP) in eV computed using DFPT in the DFT+ U + V framework for Mn(3d) states in Li_xMnPO_4 , for Fe(3d) states in Li_xFePO_4 , and for Mn(3d) and Fe(3d) in $\text{Li}_x\text{Mn}_{1/2}\text{Fe}_{1/2}\text{PO}_4$ for $x = 0, 1/4, 1/2, 3/4, 1$.

hence the U value is smaller. Also intersite Hubbard V values are decreased when going from $x = 0$ to $x = 1$. This latter fact is because the Li insertion leads to an increase of the cell volume (see Fig. S1) and of the Mn–O bond lengths; the larger the bond lengths between two atoms, the smaller is the intersite Hubbard V interaction.

It is useful to make a comparison of the Hubbard U and V values reported in Table S1 with those in Ref. [22]. In general, we find that there is a good agreement between these two studies, with largest differences for Hubbard parameters being ~ 0.3 eV in the DFT+ U + V framework. However, in the DFT+ U framework the largest difference in the Hubbard U is ~ 2 eV. These differences stem from the fact that in this paper we consistently use orthogonalized atomic orbitals for the calculation of Hubbard parameters *and* for the structural optimization (i.e. to compute Hubbard forces and stresses [13]), whereas in Ref. [22] the orthogonalized atomic orbitals were used for the calculation of Hubbard parameters while structural optimizations were based on nonorthogonalized atomic orbitals (since at that time there was no implementation of energy derivatives with orthogonal basis set.). This highlights the importance of consistency in using the same type of Hubbard projector functions across all calculations.

Finally, it is informative to comment about a change in Hubbard parameters when gradually changing the concentration of Li. We stress that Hubbard parameters are site-dependent quantities, i.e. they are *not* global averaged values that are the same for all TM ions. Interestingly, from Table S1 we can see that Hubbard U 's for different TM elements of a given material do not change in a monotonic way upon Li intercalation. This finding is consistent with Ref. [22]. In other words, the U values *do not* change in a digital manner in contrast to the Löwdin occupations in Fig. 3 of the main text. At this stage it is important to recall once more that the Hubbard parameters are computed

in a self-consistent way, i.e. by reoptimizing the crystal structure and by recomputing U and V until both the crystal and electronic structure are fully consistent with each other at each new Li concentration. Therefore, when adding one extra Li to the structure, only one TM ion receives an extra electron and thus it changes its oxidation state, but overall the whole structure readjusts such that the total energy of the system is minimized. As a result, all TM ions move slightly away from their old positions and hence their chemical environment change. As a consequence, Hubbard U and V change for all atoms and not only for the TM ion that received an extra electron.

S3. Crystal structure parameters

Figure S1 shows the lattice parameters (a , b , c), angles (α , β , γ), and the cell volume (V) of Li_xMnPO_4 , Li_xFePO_4 , and $\text{Li}_x\text{Mn}_{1/2}\text{Fe}_{1/2}\text{PO}_4$ at $x = 0, 1/4, 1/2, 3/4, 1$ computed using DFT and DFT+ U + V in comparison with experiments [23–25]. It can be seen that the lattice parameters a and b increase upon Li intercalation, while the lattice parameter c decreases. This is in agreement with the experimental trends. At $x = 1$ all computed lattice parameters are in remarkable agreement with the experimental values, with DFT+ U + V results being slightly more accurate than the DFT ones. At $x = 0$ for Li_xFePO_4 , the DFT and DFT+ U + V lattice parameters are almost the same and they somewhat overestimate the experimental ones. However, at $x = 0$ for Li_xMnPO_4 , the lattice parameter a is very similar between DFT and DFT+ U + V and it is in good agreement with experiments, while the experimental value of b is in-between the DFT and DFT+ U + V predictions, while the c parameter is overestimated in DFT and even more in DFT+ U + V [22].

The angles α , β , and γ are all 90° at $x = 0$ and $x = 1$ because the structure is orthorhombic, in agreement with experiments [23–25]. However, at intermediate Li concentrations, $x = 1/4$ and $x = 3/4$, there is a deviation from the orthorhombic symmetry both in DFT and DFT+ U + V , and the angles differ from 90° . At $x = 1/2$, there are no general trends: depending on the level of theory and on which angle is being considered we observe possible deviations from 90° .

In Fig. S1, the cell volume at different Li concentrations. The general trend is that the addition of Li expands the lattice and the cell volume increases. At $x = 1$ we find that the DFT+ U + V volumes are in remarkable agreement with the experimental ones while DFT volumes are somewhat underestimated. In contrast, at $x = 0$ we observe that both DFT and DFT+ U + V volumes overestimate the experimental one in Li_xFePO_4 , while in Li_xMnPO_4 the DFT volume is in good agreement with the experimental one while the DFT+ U + V volume is overestimated.

Overall we find that the accuracy of DFT+ U + V is fairly good for predicting the crystal structural parameters. For this reason we used the DFT+ U + V structural parameters also for the HSE06 calculations (since the HSE06 structural optimization is computationally too expensive for phospho-olivines).

S4. Population analysis for $\text{Li}_x\text{Mn}_{1/2}\text{Fe}_{1/2}\text{PO}_4$

Table S2 presents the population analysis data for the $3d$ shell of Mn and Fe atoms in $\text{Li}_x\text{Mn}_{1/2}\text{Fe}_{1/2}\text{PO}_4$ at $x = 0$ and $x = 1$ computed using four levels of theory (DFT, DFT+ U , DFT+ U + V , and HSE06) and the nominal data. More specifically, it shows the eigenvalues of the site-diagonal ($I = J$) atomic occupation matrix $n_{mm'}^{I\sigma}$ of size 5×5 [see Eq. (5) in the main text] in the spin-up ($\sigma = \uparrow : \lambda_i^\uparrow$) and spin-down ($\sigma = \downarrow : \lambda_i^\downarrow$) channels, Löwdin occupations $n = \sum_{i=1}^5 (\lambda_i^\uparrow + \lambda_i^\downarrow)$, magnetic moments $m = \sum_{i=1}^5 (\lambda_i^\uparrow - \lambda_i^\downarrow)$, and the OS determined using the method of Ref. [26].

By comparing the data in Table S2 with the one in Table I in the main text we can see that the trends are the same. In other words, in the mixed olivine $\text{Li}_x\text{Mn}_{1/2}\text{Fe}_{1/2}\text{PO}_4$, the occupations n , magnetic moments m , and eigenvalues λ_i^σ are essentially the same as in corresponding olivines Li_xFePO_4 and Li_xMnPO_4 . This means that mixing of Mn and Fe atoms in the same olivine compound does not lead to changes in their "pristine" electrochemical properties. Therefore, the discussion and the analysis presented in Sec. III.A applies also to $\text{Li}_x\text{Mn}_{1/2}\text{Fe}_{1/2}\text{PO}_4$ in exactly the same way.

By using the method of Ref. [26], the analysis of the eigenvalues of the atomic occupation matrix in Table S2 reveals that at $x = 0$ both Mn and Fe are in the $3+$ OS, while at $x = 1$ both of them are in the $2+$ OS. By performing the same analysis at intermediate Li concentrations we find that first the Mn ions change their OS from $3+$ to $2+$ (for $0 < x < 1/2$) while all Fe ions remain in the $3+$ OS, and further at $1/2 < x < 1$ the Fe ions change their OS from $3+$ to $2+$ while Mn ions remain in the $2+$ OS (see Fig. 3 in the main text).

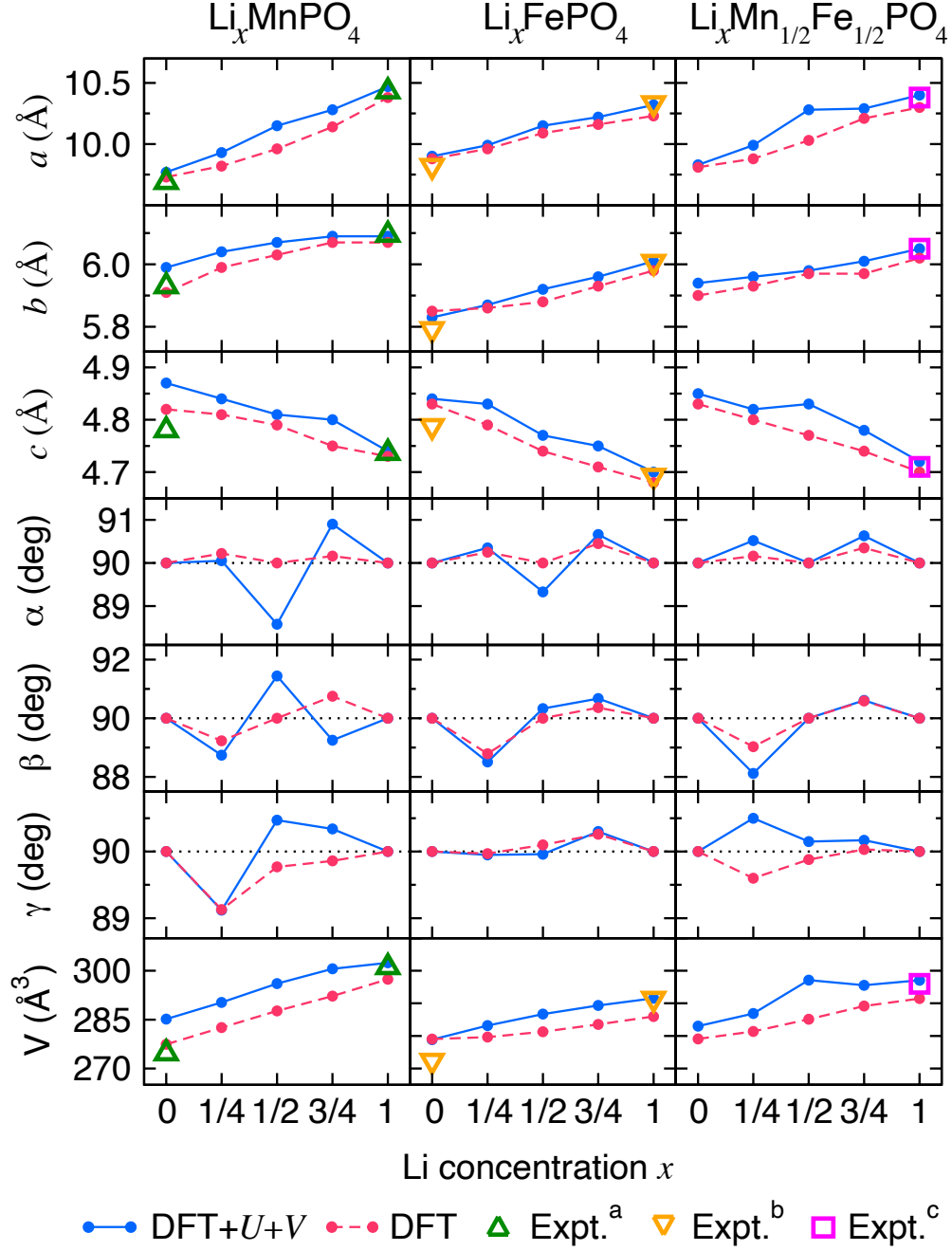


FIG. S1: Lattice parameters (a , b , c), angles (α , β , γ), and the cell volume (V) of Li_xMnPO_4 , Li_xFePO_4 , and $\text{Li}_x\text{Mn}_{1/2}\text{Fe}_{1/2}\text{PO}_4$ at $x = 0, 1/4, 1/2, 3/4, 1$ computed using DFT and DFT+ $U+V$. The experimental values are: Expt.^a is Ref. 23, Expt.^b is Ref. 24, and Expt.^c is Ref. 25.

S5. Magnetic moments

Figure S2 shows the relative magnetic moments for Mn and Fe atoms in Li_xMnPO_4 , Li_xFePO_4 , and $\text{Li}_x\text{Mn}_{1/2}\text{Fe}_{1/2}\text{PO}_4$ at $x = 0, 1/4, 1/2, 3/4, 1$ computed using three levels of theory (DFT, DFT+ $U+V$, and HSE06). The exact values of the magnetic moments at $x = 0$ and $x = 1$ are reported in Table I of the main text and in Table S2.

Method	x	Element	λ_1^\uparrow	λ_2^\uparrow	λ_3^\uparrow	λ_4^\uparrow	λ_5^\uparrow	λ_1^\downarrow	λ_2^\downarrow	λ_3^\downarrow	λ_4^\downarrow	λ_5^\downarrow	n	m (μ_B)	OS
DFT	0	Mn	0.43	0.98	0.98	0.99	1.00	0.09	0.11	0.13	0.16	0.27	5.12	3.62	3+
		Fe	0.97	0.98	0.99	1.00	1.00	0.15	0.17	0.17	0.25	0.26	5.93	3.95	3+
	1	Mn	0.98	0.99	0.99	0.99	1.00	0.03	0.04	0.05	0.11	0.11	5.28	4.61	2+
		Fe	0.99	0.99	0.99	0.99	1.00	0.06	0.07	0.13	0.14	0.98	6.32	3.57	2+
DFT+ U	0	Mn	0.54	0.99	0.99	1.00	1.00	0.04	0.05	0.06	0.09	0.19	4.95	4.10	3+
		Fe	0.99	0.99	1.00	1.00	1.00	0.08	0.11	0.11	0.21	0.24	5.72	4.22	3+
	1	Mn	0.99	0.99	1.00	1.00	1.00	0.02	0.02	0.03	0.07	0.08	5.19	4.76	2+
		Fe	0.99	0.99	1.00	1.00	1.00	0.03	0.03	0.08	0.09	1.00	6.20	3.76	2+
DFT+ U + V	0	Mn	0.50	0.99	0.99	1.00	1.00	0.05	0.06	0.08	0.10	0.22	4.98	3.98	3+
		Fe	0.99	0.99	1.00	1.00	1.00	0.09	0.13	0.13	0.21	0.24	5.76	4.18	3+
	1	Mn	0.99	0.99	1.00	1.00	1.00	0.02	0.02	0.03	0.08	0.08	5.21	4.75	2+
		Fe	0.99	0.99	1.00	1.00	1.00	0.03	0.04	0.09	0.10	0.99	6.22	3.74	2+
HSE06	0	Mn	0.40	0.99	0.99	0.99	0.99	0.06	0.07	0.08	0.11	0.23	4.91	3.83	3+
		Fe	0.99	0.99	0.99	0.99	1.00	0.08	0.11	0.11	0.19	0.22	5.67	4.26	3+
	1	Mn	0.99	0.99	1.00	1.00	1.00	0.02	0.02	0.03	0.08	0.08	5.21	4.75	2+
		Fe	0.99	0.99	1.00	1.00	1.00	0.03	0.04	0.09	0.09	0.99	6.22	3.74	2+
Nominal	0	Mn	0.00	1.00	1.00	1.00	1.00	0.00	0.00	0.00	0.00	0.00	4.00	4.00	3+
		Fe	1.00	1.00	1.00	1.00	1.00	0.00	0.00	0.00	0.00	0.00	5.00	5.00	3+
	1	Mn	1.00	1.00	1.00	1.00	1.00	0.00	0.00	0.00	0.00	0.00	5.00	5.00	2+
		Fe	1.00	1.00	1.00	1.00	1.00	0.00	0.00	0.00	0.00	1.00	6.00	4.00	2+

TABLE S2: Population analysis data for the $3d$ shell of Mn and Fe atoms in $\text{Li}_x\text{Mn}_{1/2}\text{Fe}_{1/2}\text{PO}_4$ at $x = 0$ and $x = 1$ computed using four levels of theory (DFT, DFT+ U , DFT+ U + V , and HSE06) and the nominal data. This table shows the eigenvalues of the site-diagonal occupation matrix for the spin-up (λ_i^\uparrow , $i = \overline{1}, \overline{5}$) and spin-down (λ_i^\downarrow , $i = \overline{1}, \overline{5}$) channels, Löwdin occupations $n = \sum_i (\lambda_i^\uparrow + \lambda_i^\downarrow)$, magnetic moments $m = \sum_i (\lambda_i^\uparrow - \lambda_i^\downarrow)$, and the oxidation state (OS). For the sake of simplicity we dropped the atomic site index I from all quantities reported here. The eigenvalues are written in the ascending order (from left to right) for each spin channel. The eigenvalues written in bold are considered as being such that correspond to fully occupied states and thus are taken into account when determining the OS according to Ref. [26].

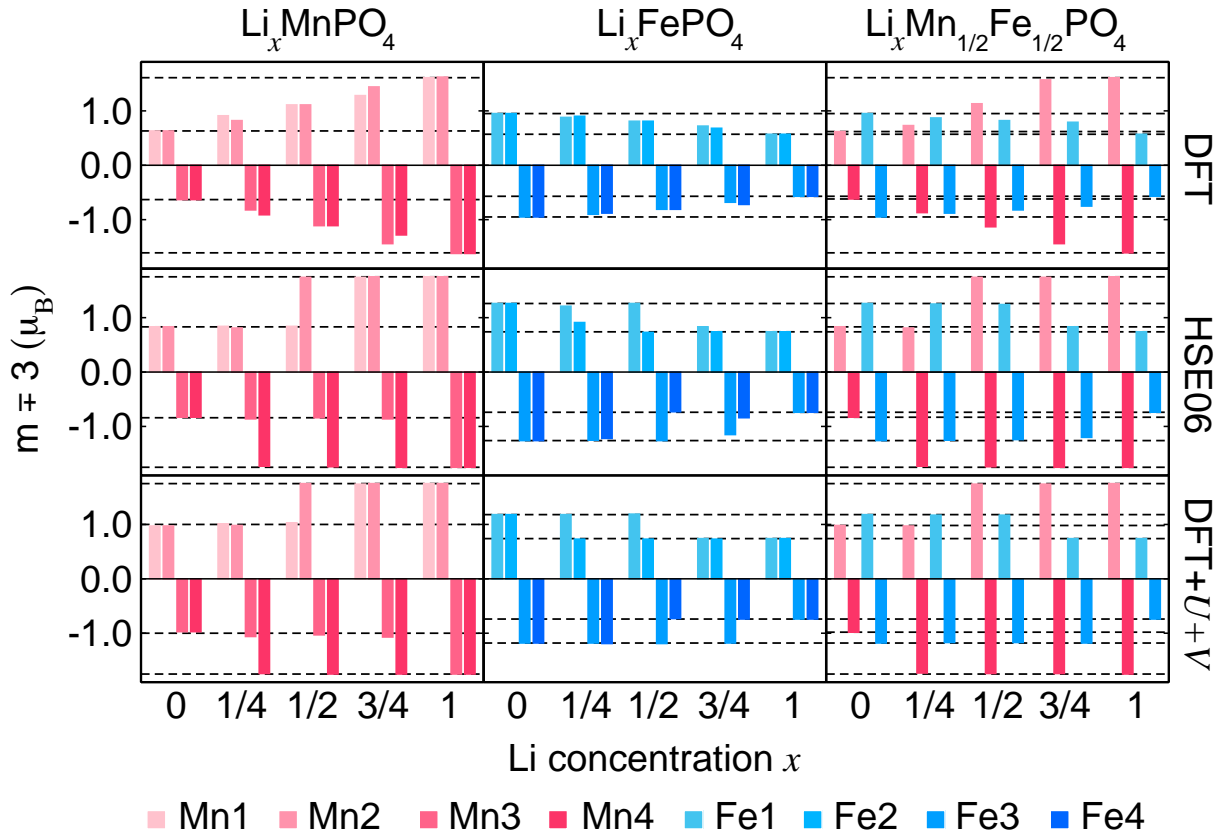


FIG. S2: Magnetic moments (shifted by $\mp 3 \mu_B$ for the sake of clearer comparison) for Mn and Fe atoms in Li_xMnPO_4 , Li_xFePO_4 , and $\text{Li}_x\text{Mn}_{1/2}\text{Fe}_{1/2}\text{PO}_4$ at $x = 0, 1/4, 1/2, 3/4, 1$ computed using three levels of theory (DFT, DFT+U+V, and HSE06). The horizontal dashed lines correspond to the magnetic moments of the end elements ($x = 0$ and $x = 1$). For each material there are four transition-metal atoms, each of which is represented with a bar.

These magnetic moments were computed via the projection method, i.e. by computing the atomic occupation matrix [see Eq. 5 in the main text], then by diagonalizing it, and eventually by computing $m = \sum_{i=1}^5 (\lambda_i^\uparrow - \lambda_i^\downarrow)$ using the data in Table S2.

Before we proceed to the detailed analysis of Fig. S2, it is useful to compare the computed magnetic moments with the available experimental values. On the one hand, for Li_xMnPO_4 , at $x = 0$ the experimental magnetic moments are not known to the best of our knowledge, while at $x = 1$ they are 4.28 [27] and 5.20 μ_B [28]. These experimental values are largely scattered which complicates a comparison with our theoretical predictions. Nevertheless, from Table I in the main text we can see that both DFT+ U + V and HSE06 predict the magnetic moment to be 4.75 μ_B which falls right between the two experimental values. The predictions by DFT and DFT+ U are 4.62 and 4.76 μ_B , respectively, which also fall between the experimental values. On the other hand, for Li_xFePO_4 , at $x = 0$ the experimental magnetic moment is 4.15 μ_B while at $x = 1$ it is 4.19 μ_B [29]. At $x = 0$, DFT+ U + V and HSE06 predict the magnetic moments to be 4.18 and 4.26 μ_B , respectively, and at $x = 1$ the magnetic moments are 3.74 from both methods. The DFT and DFT+ U magnetic moments give quite similar values (see Table I in the main text). Therefore, at $x = 0$, the DFT+ U + V magnetic moment falls between the two experimental values and it makes this method more accurate than HSE06 and other other methods considered here. However, at $x = 1$ the computed magnetic moments are smaller than in experiments. Most importantly, we find that the trend when going from $x = 0$ to $x = 1$ is the opposite in experiments and in simulations. It would be important to have novel and more accurate experiments on Li_xFePO_4 to verify whether the trend of Ref. [29] is correct. Finally, we are not aware of the experimental magnetic moments in $\text{Li}_x\text{Mn}_{1/2}\text{Fe}_{1/2}\text{PO}_4$.

Now let us discuss Fig. S2. Our main goal here (as in the main text for Löwdin occupations) is to compare the accuracy of the DFT+ U + V approach versus HSE06 for predicting a relative change in magnetic moments upon lithiation of phospho-olivines. In the case of Li_xMnPO_4 , we can see that DFT+ U + V and HSE06 agree remarkably well and both show a digital change in the magnetic moments: adding one Li^+ ion and one electron to the cathode during the lithiation process leads to the change in the magnetic moment of only one Mn ion (that accepts this extra electron) while all other Mn ions remain unchanged. This process continues when we go on with the Li intercalation until eventually all Mn ions change their magnetic moments from smaller to larger (by modulus). Thus, these two approaches successfully describe the mixed-valence nature of the Li_xMnPO_4 compound that contains two types of Mn ions, Mn^{3+} and Mn^{2+} , at $x = 1/4, 1/2, 3/4$. In contrast, DFT fails to localize an extra electron on one of the Mn ions and as a consequence the charge density is spread out and equally distributed among all Mn ions in the system which breaks the digital change in magnetic moments. In the case of Li_xFePO_4 , the findings are similar with a difference that here only DFT+ U + V shows the digital change in the magnetic moments while HSE06 does not manage to do so accurately. Finally, in $\text{Li}_x\text{Mn}_{1/2}\text{Fe}_{1/2}\text{PO}_4$ we find that both DFT+ U + V and HSE06 agree to describe the change in the magnetic moments on Mn ions in a digital manner, while for Fe ions again we find that DFT+ U + V is more accurate than HSE06.

S6. Projected density of states for Li_xMnPO_4 and Li_xFePO_4

Figures S3 and S4 show the spin-resolved PDOS for Li_xMnPO_4 and Li_xFePO_4 at different concentrations of Li ($x = 0, 1/4, 1/2, 3/4, 1$) using three levels of theory (DFT, DFT+ U + V , and HSE06). The observations are similar to those presented for $\text{Li}_x\text{Mn}_{1/2}\text{Fe}_{1/2}\text{PO}_4$ in Sec. III.B in the main text. For both materials, Li_xMnPO_4 and Li_xFePO_4 , DFT fails to predict the correct change in the PDOS during the lithiation process due to SIE, i.e. at fractional x there is no evidence that only one TM element changes its OS from 3+ to 2+. Conversely, both DFT+ U + V and HSE06 show correct trends for these phospho-olivines. More specifically, when gradually adding Li ions to the materials, we see that only one TM elements changes its OS from 3+ to 2+ which is seen in the shifts of the corresponding Mn-3d or Fe-3d states. The overall similarity in PDOS from DFT+ U + V and HSE06 is striking, thought as is discussed in the main text for $\text{Li}_x\text{Mn}_{1/2}\text{Fe}_{1/2}\text{PO}_4$ the fine details differ. In particular, the distribution of occupied states near the top of the valence bands is quite different withing these two approaches: the intensity of the Mn-3d states in the case of Li_xMnPO_4 and of Fe-3d states in the case of Li_xFePO_4 is higher in HSE06, and there is a gap between them at $x = 1$. As we pointed out in the main text, in order to check which one of these two levels of theory is more accurate in predicting the true electronic structure of the phospho-olivines one would need to make comparisons with photoemission and X-ray absorption spectroscopy measurements which are not available at present.

S7. Band gaps

Figure S5 shows the band gaps for Li_xMnPO_4 , Li_xFePO_4 , and $\text{Li}_x\text{Mn}_{1/2}\text{Fe}_{1/2}\text{PO}_4$ computed using four levels of theory (DFT, DFT+ U , DFT+ U + V , and HSE06) and as measured in experiments [30, 31]. It can be seen that

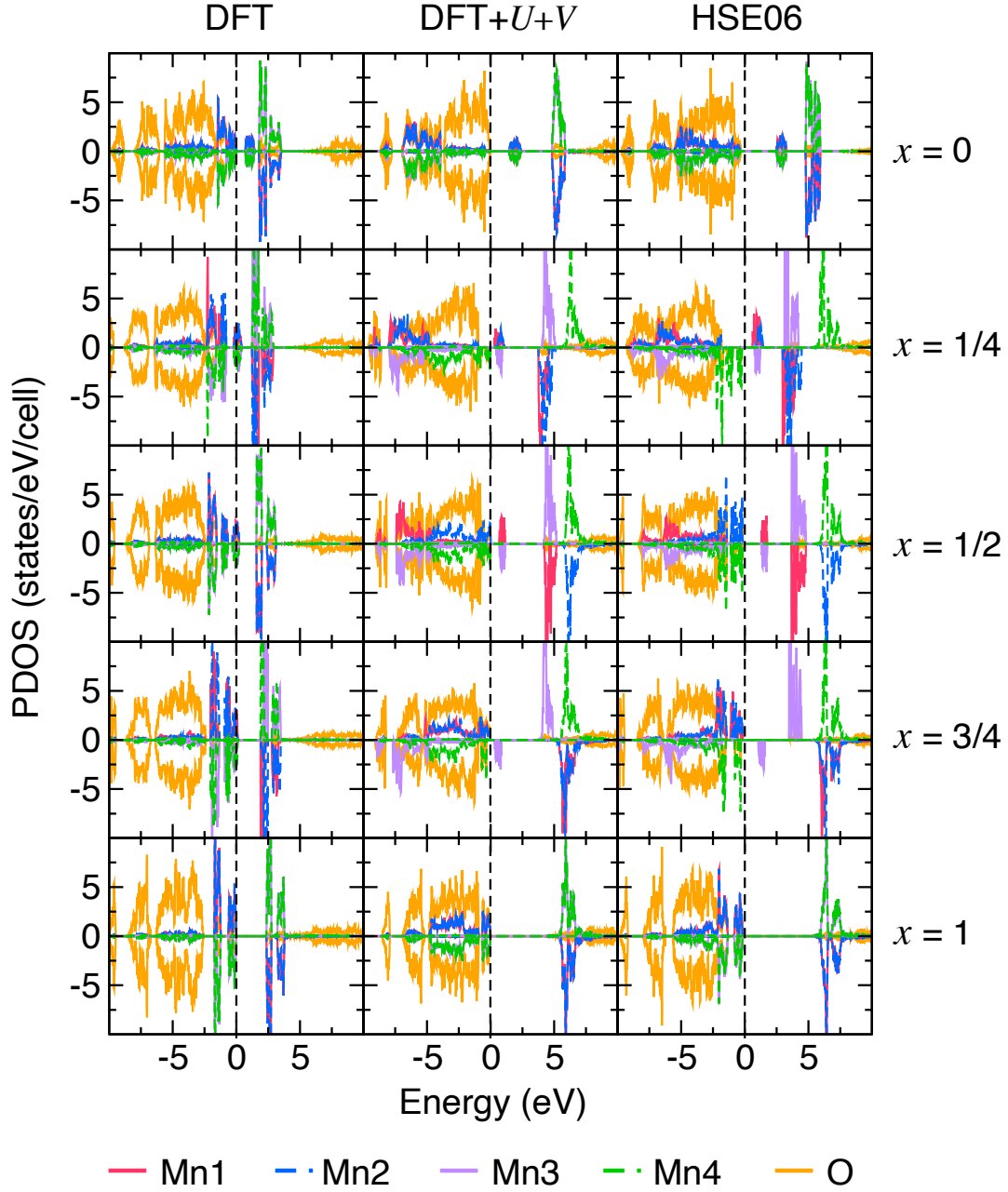


FIG. S3: Spin-resolved PDOS in Li_xMnPO_4 at different concentrations of Li ($x = 0, 1/4, 1/2, 3/4, 1$) for $3d$ states of Mn1, Mn2, Mn3, Mn4 and for $2p$ states of O, computed using DFT, DFT+ $U+V$, and HSE06. The PDOS for O- $2p$ states was obtained by summing up contributions from all O atoms in the simulation cell and it was multiplied by a factor of $1/2$ in order to have clearer comparison with the PDOS of Mn atoms. The zero of energy corresponds to the top of the valence bands in the case of insulating ground states or the Fermi level in the case of metallic ground states. The upper part of each panel corresponds to the spin-up channel, and the lower part corresponds to the spin-down channel.

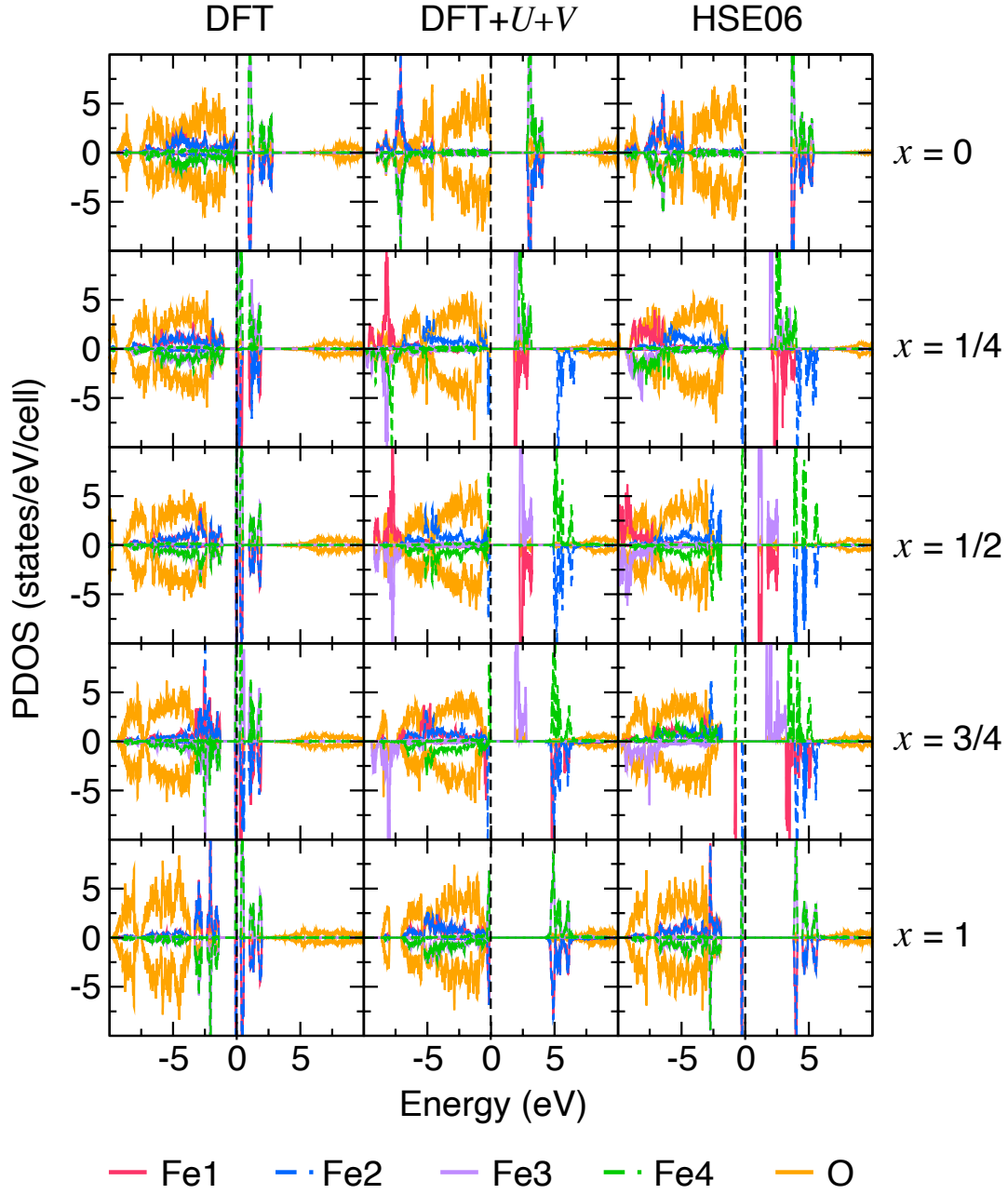


FIG. S4: Spin-resolved PDOS in Li_xFePO_4 at different concentrations of Li ($x = 0, 1/4, 1/2, 3/4, 1$) for $3d$ states of Fe1, Fe2, Fe3, Fe4 and for $2p$ states of O, computed using DFT, DFT+ $U+V$, and HSE06. The PDOS for O- $2p$ states was obtained by summing up contributions from all O atoms in the simulation cell and it was multiplied by a factor of $1/2$ in order to have clearer comparison with the PDOS of Fe atoms. The zero of energy corresponds to the top of the valence bands in the case of insulating ground states or the Fermi level in the case of metallic ground states. The upper part of each panel corresponds to the spin-up channel, and the lower part corresponds to the spin-down channel.

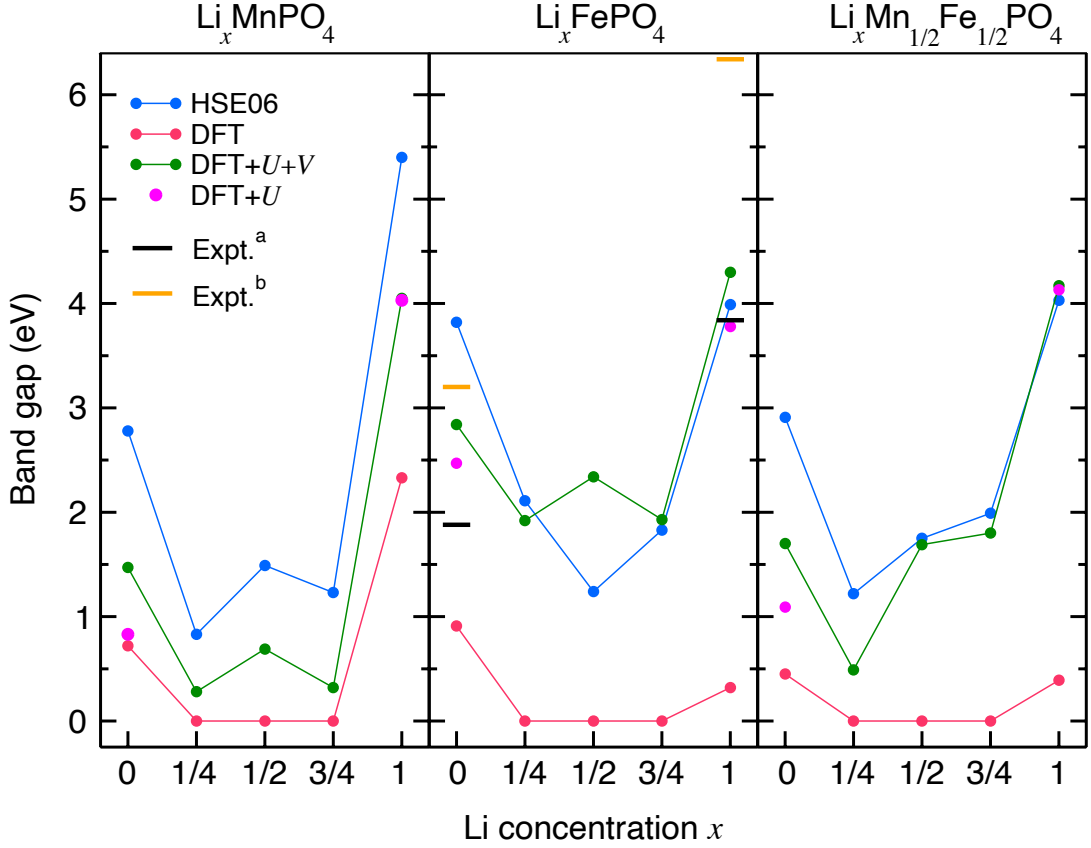


FIG. S5: Band gaps for Li_xMnPO_4 , Li_xFePO_4 , and $\text{Li}_x\text{Mn}_{1/2}\text{Fe}_{1/2}\text{PO}_4$ computed using four levels of theory (DFT, DFT+ U , DFT+ U + V , and HSE06) and as measured in experiments: Expt.^a is Ref. [30], Expt.^b is Ref. [31].

the values of band gaps are very sensitive to the level of theory that is used. Unfortunately, the availability of the experimental studies of band gaps in these materials is very scarce, which makes it almost impossible to verify which level of theory is the most accurate in predicting the band gaps. We have found the experimental values of band gaps only for Li_xFePO_4 at $x = 0$ and $x = 1$ [30, 31], and these values differ largely. Based on this data we can see that at $x = 0$ the DFT+ U and DFT+ U + V predictions fall in-between the two experimental values while the HSE06 band gap overestimates both of them. At $x = 1$ we see that the DFT+ U , DFT+ U + V , and HSE06 band gaps are all close to the experimental values of Ref. [30], while the experimental value of Ref. [31] is larger by ~ 2 eV. Therefore, there is a call for more experiments on accurate determination of band gaps in these phospho-olivines.

It is useful to compare general trends in changes of the band gap upon the lithiation of these cathode materials. We observe that the DFT+ U + V and HSE06 band gaps behave quite similarly when changing x . However, in Li_xMnPO_4 we can see there is approximately a rigid downward-in-energy shift of the DFT+ U + V band gaps compared to the HSE06 ones. Instead, in Li_xFePO_4 the DFT+ U + V and HSE06 band gaps are very close at $x = 1/4, 3/4, 1$ while at $x = 0$ and $x = 1$ they differ by ~ 1 eV. In $\text{Li}_x\text{Mn}_{1/2}\text{Fe}_{1/2}\text{PO}_4$ the DFT+ U + V and HSE06 band gaps agree closely at $x = 1/2, 3/4, 1$ while at $x = 0$ and $x = 1/4$ they differ by ~ 1 eV. Hence, we find that there is no general trend in band gap differences at various x when using DFT+ U + V and HSE06 for different phospho-olivines. The DFT+ U band gaps at $x = 0$ and $x = 1$ for different phospho-olivines are generally smaller than the DFT+ U + V ones, with a few exceptions when the two match (i.e. at $x = 1$ for Li_xMnPO_4 and $\text{Li}_x\text{Mn}_{1/2}\text{Fe}_{1/2}\text{PO}_4$). Finally, the DFT predictions of band gaps differ notably from those of DFT+ U + V and HSE06: at fractional x all materials are predicted to be metallic. This failure of DFT is due to the fact that Mn-3d and Fe-3d electrons are overdelocalized due to SIE and hence this leads to the closure of the gap.

-
- [1] P. Giannozzi, S. Baroni, N. Bonini, M. Calandra, R. Car, C. Cavazzoni, D. Ceresoli, G. Chiarotti, M. Cococcioni, I. Dabo, A. Dal Corso, S. De Gironcoli, S. Fabris, G. Fratesi, R. Gebauer, U. Gerstmann, C. Gougoussis, A. Kokalj, M. Lazzeri, L. Martin-Samos, N. Marzari, F. Mauri, R. Mazzarello, S. Paolini, A. Pasquarello, L. Paulatto, C. Sbraccia, S. Scandolo, G. Sclauzero, A. Seitsonen, A. Smogunov, P. Umari, and R. Wentzcovitch, Quantum ESPRESSO: A modular and open-source software project for quantum simulations of materials, *J. Phys.: Condens. Matter* **21**, 395502 (2009).
 - [2] P. Giannozzi, O. Andreussi, T. Brumme, O. Bunau, M. Buongiorno Nardelli, M. Calandra, R. Car, C. Cavazzoni, D. Ceresoli, M. Cococcioni, N. Colonna, I. Carnimeo, A. Dal Corso, S. de Gironcoli, P. Delugas, R. A. DiStasio Jr., A. Ferretti, A. Floris, G. Fratesi, G. Fugallo, R. Gebauer, U. Gerstmann, F. Giustino, T. Gorni, J. Jia, M. Kawamura, H.-Y. Ko, A. Kokalj, E. Küçükbenli, M. Lazzeri, M. Marsili, N. Marzari, F. Mauri, N. L. Nguyen, H.-V. Nguyen, A. Otero-de-la Rosa, L. Paulatto, S. Poncé, D. Rocca, R. Sabatini, B. Santra, M. Schlipf, A. Seitsonen, A. Smogunov, I. Timrov, T. Thonhauser, P. Umari, N. Vast, and S. Baroni, Advanced capabilities for materials modelling with Quantum ESPRESSO, *J. Phys.: Condens. Matter* **29**, 465901 (2017).
 - [3] P. Giannozzi, O. Baseggio, P. Bonfà, D. Brunato, R. Car, I. Carnimeo, C. Cavazzoni, S. de Gironcoli, P. Delugas, F. Ferrari Ruffino, A. Ferretti, N. Marzari, I. Timrov, A. Urru, and S. Baroni, Quantum ESPRESSO toward the exascale, *J. Chem. Phys.* **152**, 154105 (2020).
 - [4] J. Perdew, A. Ruzsinszky, G. Csonka, O. Vydrov, G. Scuseria, L. Constantin, X. Zhou, and K. Burke, *Phys. Rev. Lett.* **100**, 136406 (2008).
 - [5] G. Prandini, A. Marrazzo, I. E. Castelli, N. Mounet, and N. Marzari, Precision and efficiency in solid-state pseudopotential calculations, *npj Computational Materials* **4**, 1 (2018).
 - [6] The SSSP library of the Materials Cloud: <https://www.materialscloud.org/discover/sssp/table/precision>.
 - [7] K. Garrity, J. Bennett, K. Rabe, and D. Vanderbilt, *Comput. Mater. Sci.* **81**, 446 (2014).
 - [8] E. Kucukbenli, M. Monni, B. Adetunji, X. Ge, G. Adebayo, N. Marzari, S. de Gironcoli, and A. Dal Corso, Projector augmented-wave and all-electron calculations across the periodic table: a comparison of structural and energetic properties, arXiv:1404.3015 (2014).
 - [9] A. Dal Corso, Pseudopotentials periodic table: From H to Pu, *Comput. Mater. Sci.* **95**, 337 (2014).
 - [10] M. van Setten, M. Giantomassi, E. Bousquet, M. Verstraete, D. Hamann, X. Gonze, and G.-M. Rignanese, The PSEUDO-DOJO: Training and grading a 85 element optimized norm-conserving pseudopotential table, *Comput. Phys. Commun.* **226**, 39 (2018).
 - [11] P.-O. Löwdin, On the Non-Orthogonality Problem Connected with the Use of Atomic Wave Functions in the Theory of Molecules and Crystals, *J. Chem. Phys.* **18**, 365 (1950).
 - [12] I. Mayer, On Löwdin's method of symmetric orthogonalization, *Int. J. Quant. Chem.* **90**, 63 (2002).
 - [13] I. Timrov, F. Aquilante, L. Binci, M. Cococcioni, and N. Marzari, Pulay forces in density-functional theory with extended Hubbard functionals: from nonorthogonalized to orthogonalized manifolds, *Phys. Rev. B* **102**, 235159 (2020).
 - [14] R. Fletcher, *Practical Methods of Optimization*, 2nd ed. (Wiley, Chichester, 1987).
 - [15] N. Marzari, D. Vanderbilt, A. De Vita, and M. Payne, *Phys. Rev. Lett.* **82**, 3296 (1999).
 - [16] I. Timrov, N. Marzari, and M. Cococcioni, HP – A code for the calculation of Hubbard parameters using density-functional perturbation theory, submitted (2022).
 - [17] M. Payne, M. Teter, D. Allen, T. Arias, and J. Joannopoulos, *Rev. Mod. Phys.* **64**, 1045 (1992).
 - [18] D. Johnson, *Phys. Rev. B* **38**, 12807 (1988).
 - [19] I. Timrov, N. Marzari, and M. Cococcioni, Hubbard parameters from density-functional perturbation theory, *Phys. Rev. B* **98**, 085127 (2018).
 - [20] F. Gygi and A. Baldereschi, Self-consistent Hartree-Fock and screened-exchange calculations in solids: Application to silicon, *Phys. Rev. B* **34**, 4405(R) (1986).
 - [21] I. Timrov, N. Marzari, and M. Cococcioni, Self-consistent Hubbard parameters from density-functional perturbation theory in the ultrasoft and projector-augmented wave formulations, *Phys. Rev. B* **103**, 045141 (2021).
 - [22] M. Cococcioni and N. Marzari, Energetics and cathode voltages of LiMPO_4 olivines ($M=\text{Fe, Mn}$) from extended Hubbard functionals, *Phys. Rev. Materials* **3**, 033801 (2019).
 - [23] Z. Nie, C. Ouyang, J. Chen, Z. Zhong, Y. Du, D. Liu, S. Shi, and M. Lei, First principles study of Jahn-Teller effects in Li_xMnPO_4 , *Solid State Commun.* **150**, 40 (2010).
 - [24] A. Padhi, K. Nanjundaswamy, and J. Goodenough, Phospho-olivines as Positive-Electrode Materials for Rechargeable Lithium Batteries, *J. Electrochem. Soc.* **144**, 1188 (1997).
 - [25] T. Muraliganth and A. Manthiram, Understanding the Shifts in the Redox Potentials of Olivines $\text{LiM}_{1-y}\text{M}_y\text{PO}_4$ ($M = \text{Fe, Mn, Co, and Mg}$) Solid Solution Cathodes, *J. Phys. Chem. C* **114**, 15530 (2010).
 - [26] P. H.-L. Sit, R. Car, M. H. Cohen, and A. Selloni, Simple, Unambiguous Theoretical Approach to Oxidation State Determination via First-Principles Calculations, *Inorg. Chem.* **50**, 10259 (2011).
 - [27] S. Gnewuch and E. Rodriguez, Distinguishing the Intrinsic Antiferromagnetism in Polycrystalline LiCoPO_4 and LiMnPO_4 Olivines, *Inorg. Chem.* **59**, 5883 (2020).
 - [28] R. Newnham, R. Santoro, and M. Redman, Neutron-diffraction study of LiMnPO_4 , *J. Phys. Chem. Solids* **26**, 445 (1965).
 - [29] G. Rousse, J. Rodriguez-Carvajal, S. Patoux, and C. Masquelier, Magnetic Structures of the Triphylite LiFePO_4 and of Its Delithiated Form FePO_4 , *Chem. Mater.* **15**, 4082 (2003).
 - [30] K. Zaghib, A. Mauger, J. Goodenough, F. Gendron, and C. Julien, Electronic, Optical, and Magnetic Properties of

- LiFePO₄: Small Magnetic Polaron Effects, Chem. Mater. **19**, 3740 (2007).
- [31] Y. Zhang, J. Alarco, A. Best, G. Snook, P. Talbot, and J. Nerkar, Re-evaluation of experimental measurements for the validation of electronic band structure calculations for LiFePO₄ and FePO₄, RSC Advances **9**, 1134 (2019).